UNIVERSITY OF CALIFORNIA,
IRVINE

Analytical and experimental investigations on non-uniform rotational distortion (NURD) correction

THESIS

submitted in partial satisfaction of the requirements
for the degree of

MASTER OF SCIENCE

IN ENGINEERING

by

Ahmad Shirazi

Thesis Committee:
Professor Zhongping Chen, Chair
Professor James Earthman
Professor Bruce J. Tromberg

2017

DEDICATION

I would like to dedicate my work to my family and, in particular, to my parents Ameneh Alipoor and Azizolah Shirazi, who instilled in me the love of learning and hard work from an early age. Thanks to you for your support and encouragement during all endeavors of my life.

TABLE OF CONTENTS

LIST OF FIGURES

LIST OF TABLES

ACKNOWLEDGMENTS

I would like to express my deep appreciation to a number of people without whom this thesis might not have been written.

To my supervisor Prof. Zhongping Chen, who generously supported my studies during the period of this research and opened a new door to explore new topics in the area of medical imaging and medical device manufacturing. He gave me the chance to develop my own ideas and at the same time kindly advised me on choosing the best route in the face of difficulties.

To the Henry Samueli School of Engineering faculty from whom I learned a lot of interesting topics in the area of advanced materials and manufacturing and their medical applications. Namely, I would like to truly thank Prof. James Earthman and Dr. Lawrence Kulinsky who were incredibly kind and generous in putting enough time and attention whenever I asked for it and cheered me on, when I was discouraged. Also, I would like to thank Prof. Bruce Tromberg for his warm attitude and for the fascinating lessons that I leaned in the area of biomedical imaging in his class.

And finally to my lab members who were always kind and supportive. In particular, I would like to thank Rachel Qu, Emon Heydari and Yusi Miao for sharing their ideas with me and walking me through unknown areas of OCT imaging and providing the required materials and equipment many times during this research.

ABSTRACT OF THE THESIS

Analytical and experimental investigations on non-uniform rotational distortion (NURD) correction

By

Ahmad Shirazi

Master of Science in Engineering

University of California, Irvine, 2017

Professor Zhongping Chen, Chair

In this study, the efforts conducted in suppressing the effects of NURD on acquired OCT images are described. The work is divided into theoretical and experimental sections. A part of the theoretical work is focused on reconstruction of a dynamic programming method that was previously used for NURD correction and implementing it in correcting the current data. Finite element analysis of the press fitting method with ABAQUS software is another portion of the theoretical work in this study. The image post-processing algorithm was validated based on a statistical method and using sets of data from an in vivo model. It made a significant difference between images before and after correction.

Experimental work mainly focused on improving the quality of probes by making them shorter and more axially symmetric. Four different potential methods were considered during the experiments with the main focus on their feasibility and reliability. The newly developed press fitting method in manufacturing of the probes was considered to be the most promising approach because it is clean, fast, strong and repeatable.

1 INTRODUCTION

1.1 Optical coherent tomography imaging

Optical Coherence Tomography (OCT) is an imaging technique that provides high resolution images of biological tissues, and it is the latest development in intravascular coronary imaging. Precision of OCT in imaging of the more superficial layers of the arterial wall makes it the method of choice for analysis of atheromatous plaque and assessment of coronary stents [1]. It considers the coherence properties of light to image micro-structures with resolution in the range of few micrometers. Standard OCT operates using broadband and continuous wave light in the visible and near-infrared spectrum. OCT images are obtained by measuring the time delay and the intensity of backscattered or back-reflected light from the sample under investigation [2].

Similar to intravascular ultrasound (IVUS), OCT provides cross-sectional images of the vessel. But instead of sound, OCT implements light for tissue analysis that enables visualization of the coronary lesions. It is important to note that the speed of light is much faster than that of sound. Therefore, interferometry techniques are necessary to measure the backscattered signal since a direct quantification cannot be achieved on such a time scale. The interferometer uses a fiber optic coupler similar to a beam splitter, which directs one-half of the beam to the object to be imaged and the other half to the reference arm.

There are mainly two types of OCT imaging systems referred to as Time Domain OCT (TD-OCT) and Frequency Domain OCT (FD OCT). A TD-OCT system consists of a mirror moving at calibrated distances to produce known echo delays. The reflected signal returning from the

tissue and reference arms are recombined in the fiber-coupler, and the interference fringes are detected by a photo detector. FD-OCT allows the simultaneous detection of reflections from all echo time delays. Therefore, it does not need a moving mirror and, in each data acquisition step, acquires data for the whole A-line instead of a pixel in the A-line which makes the system significantly faster. A general configuration of time domain (A) and frequency domain (B) OCT systems is shown in Figure 1 [3].

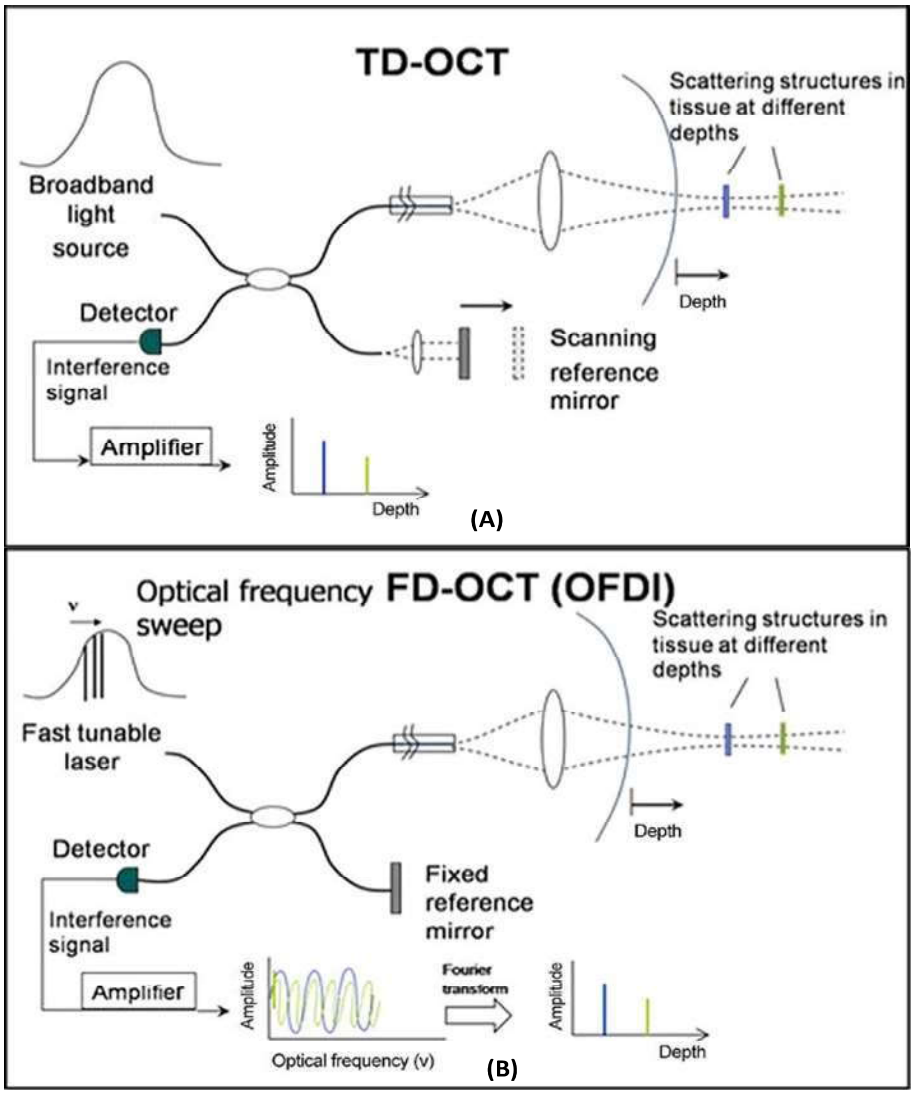

Figure 1: Typical configuration of intravascular OCT imaging for time domain (A) and frequency domain (B) [3].

The geometric fidelity of beam scanning is critical for image quality. Inaccurate scanning can introduce deformations in the image that can complicate the interpretation of clinical data. This is particularly problematic in the case of catheter-based imaging when accessing internal organs through narrow diameter, flexible fiber-optic probes. This imaging technology has some limitations and pitfalls that need to be understood before the field of application can be extended. A brief review over some of main reasons of these artifacts that happen during imaging is mentioned in the following section.

1.2 Image artifacts:

1.2.1 Movement artifacts

Motion or sew-up artifacts show themselves as a single radius of misalignment in the circumferential image and happen due to the sudden movement of the artery or imaging probe [4]. The probe is very mobile within the coronary artery, which itself moves over the cardiac cycle. Any sudden movement of the fiber-optic with respect to the artery causes an artificial break in parietal continuity. On axial reconstruction, this shows up as oscillation with the same pattern as the heart beat**.** Algorithms could be developed to correct such artifacts and reduce the risk of false diagnosis of rupture. Faster pullback and acquisition are other ways of reducing the effect of this phenomenon [5]. Figure 2-A shows a typical movement artifact in the OCT imaging.

1.2.2 Non-Uniform Rotational Distortion (NURD)

This artifact appears as a blur and unclear portion within an arc of the circumferential OCT image. It most commonly occurs in the tortuous blood vessels, tight stenosis, heavy calcification,

or equipment imperfection that perturbs the smooth rotation of the probe tip, resulting in variation in the rotational speed of the image catheter [4]. NURD is not stable in time because it depends not only on the particular probe but on its geometric configuration and the particular path inside tortuous cavities in the body, both of which change dynamically with patient movement and pullback position. Also, there might be an abrupt jump between two angular positions due to stick-and-release condition or a gradual stretch or compression due to gradual increase and decrease in friction on the probe tip [6]. New catheters have been envisioned to reduce this effect by placing a micromotor at the tip of the probe, directly rotating the optical assembly. However, it has been found that even in this case, NURD persists due to the difficulty in fabricating micromotors that are perfectly balanced [7]. In all cases, non-deterministic inter-frame NURD variations inhibit a calibration-based approach.

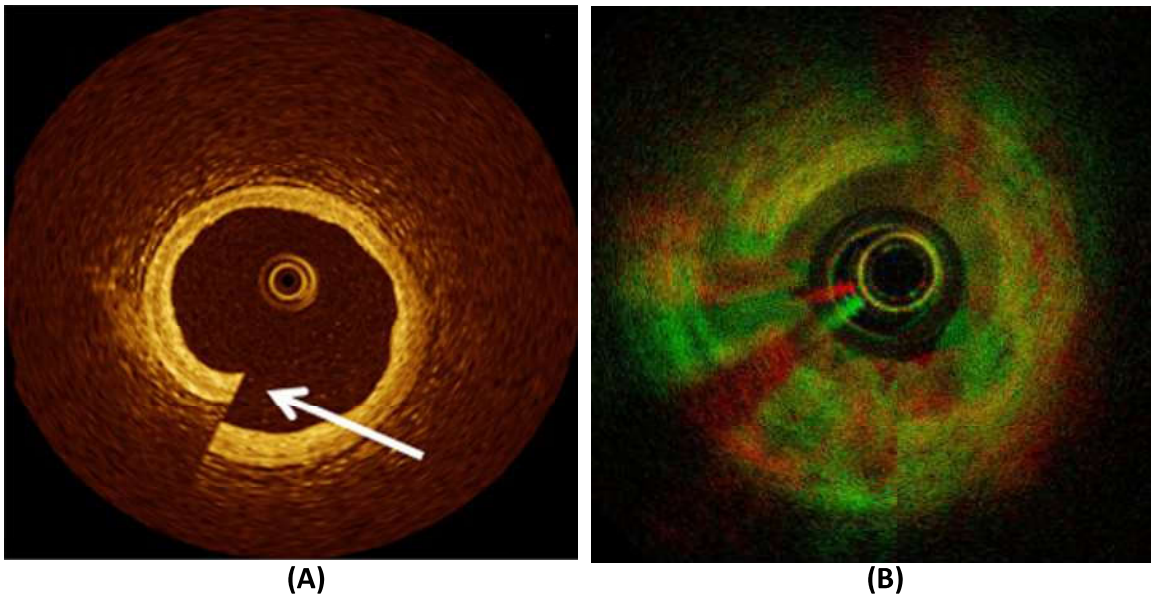

Figure 2: (A) Movement artifact [5] and (B) NURD artifact in OCT imaging.

In case of proximal probe rotation with external source of rotation, the length of the rigid portion of the probe tip, the difference between the probe diameter and internal diameter of the sheath

and axial symmetry of the probe tip are among the main controllable parameters that affect the occurrence of NURD. This artifact is illustrated in Figure 2-B.

1.2.3 Fiber decentration in large-caliber arteries

This kind of artifact can cause proximity pitfalls that happen when the imaging catheter is near or touching the artery wall which in turn cause the nearby tissue to appear brighter or more signal rich [4]. During intravascular OCT imaging, the probe does not always lie in the center of the vessel or is not pulled back parallel to the axis of the blood vessel, and this deforms the cross-sectional image, which is perpendicular to the fiber axis. Furthermore, the light signal is especially intense in regions close to the light source and attenuated in more remote regions (Figure 3-A). These artifacts are limited by the fiber-optic being contained in the inflated coaxial balloon during acquisition and are a significant source of artifacts in large blood vessels [8]. Thus, they happen to be rare when the vessel under exploration is straight (left anterior) while the angularities of the right coronary artery are highly subject to this kind of artifact. Since the data for remote areas is lost in some cases, there is not much that can be done for reconstruction of this data. However, better analysis of fiber geometry with respect to the lumen could enable such deformations to be corrected; such algorithmic correction could hardly be feasible in real time but might be applied in post-processing of certain stent parameters [5].

1.2.4 Flush quality artifacts

If there is residual blood due to suboptimal flushing, it induces a significant swirling pattern within the lumen and can be mistakenly identified as red thrombus. Also, it can limit the characterization of the underlying tissue due to high OCT signal attenuation of red blood cells [4,

9]. OCT image quality also depends on the quality of the flush, which will not be perfect when the upstream diameter makes the balloon less than fully occlusive or in case of collaterality. A few attempts at acquisition without proximal occlusion, on the other hand, proved disappointing, with insufficient flush and images that were often less usable. To prevent risks, such as myocardial ischemia, happening as a result of the disruption to blood flow in the artery, the allowed time for keeping blood off of the OCT imaging area is as short as a few seconds, which in turn limits the volume of artery that can be safely imaged with OCT [10]. An animal study also confirmed that image quality depended on arterial caliber and that flush quality was much improved by occlusion. Automatic injection should improve flush, but the future lies rather in shorter flush times and faster pullback, as with the new generation of fiber-optics [5].

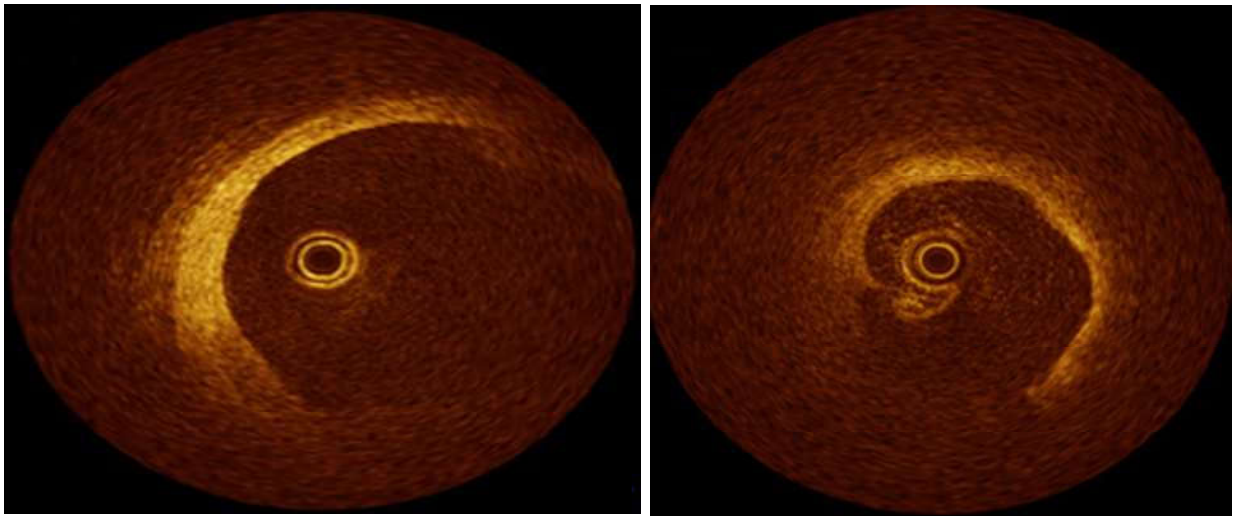

Figure 3: (A) Fiber decentration in large caliber arteries and (B) flush quality artifact [5].

1.3 Non-Uniform Rotational Distortion (NURD)

Catheters based OCT has a two dimensional scanning mechanisms: a longitudinal motion (pullback) and an azimuthal (angular) rotational motion. Catheters need to be highly flexible to be able to be used in anatomical tortuous pathes and to enable manipulation during the

procedure. There is a necessary trade-off with the fidelity of torque and translation transfer. The image distortions that result from scanning inaccuracy are commonly referred to as non-uniform rotation distortion (NURD) in the medical imaging community [11].

NURD is a common problem in catheter-based imaging systems such as intravascular and endoscopic OCT. The probe is proximally actuated in common OCT scanning systems with an external rotary motor. In these systems, NURD is observed for both in vivo and ex vivo studies, suggesting that it is present regardless of body motion and other physiological concerns due to mechanical friction between the catheter torque coil (TC) and sheath [12]. Physiological motion as well as bends encountered in endoscopic and cardiovascular imaging applications can still have a great impact on the severity of the rotational non-uniformity. Some of above mentioned issues are related to proximal rotation and, therefore, the micromotor catheter technology that performs distal rotational scanning can improve the imaging process [13]. Nevertheless, NURD still exists due to manufacturing imperfections and motor mechanical instability. Although this can be overcome by using any kind of close loop control, such as encoders, it will increase the size of probe which might not allow it to be used for clinical applications [14].

NURD is a well documented topic for Intravascular Ultrasound imaging (IVUS); however, there are few papers that have focused on NURD in OCT imaging. It can be both due to the reduced severity of NURD in OCT in comparison with IVUS imaging [11] or due to undefined nature of the artifact [7]. Nevertheless, methods used for NURD detection in IVUS can be implemented in OCT image processing. There are different methods to approach NURD that can be mainly categorized into two groups.

The first group includes methods that use cross correlation between neighboring A-lines or frames or certain blocks of different frames to estimate the NURD and angular distortion. Considering different imaging blocks at [15], cross correlations between them in different IVUS frames are used to track tissue motion. Also in [11], a technique that uses frequency analysis of the texture of the IVUS image to estimate the rotational speed is described. Similarity between frames for correction of NURD in OCT is also described in [16]. All feature-based techniques share the same main drawback: they need a reference frame with no NURD or at least zero-mean NURD in the whole data set. Otherwise, they will not only correct for relative NURD between frames but also propagate NURD present in the reference frame. In addition, successful matches at all azimuthal positions for faithful tracking are not guaranteed. These methods require multiple frames in memory and have non-deterministic processing times which complicate their implementation for real-time correction. In addition, methods using cross-correlation or phase information typically require highly correlated images. Some methods require disabling the longitudinal scan (pullback) entirely or provide only moderate improvement in rotational uniformity when tested in vivo [17]. When there is significant patient or operator motion, methods that do not rely on feature-based imaging methods for correction may be desirable, due to change of tissue features as a result of physiological motions.

The second category belongs to methods that take advantage of fiducial (spatially fixed) features to correct for NURD. Using structural landmarks (e.g., stent struts) to help registration of subsequently acquired datasets is performed in reference [18]. Also the reflections from the sheath or optical components of the catheters and using the fixed struts that hold the structure of the micromotor as fiducials for detecting NURD in micromotor catheters [12] are examples of these methods. But these approaches provided only a low time-resolution measure of speed, and

unobstructed circumferential imaging is preferred. In what follows, recent works that are directly concentrated on NURD correction in OCT imaging are briefly discussed.

A model for prediction of NURD and determining the effect of different parameters on it is presented in [19]. A square geometry instead of the circular shape of an artery is used to simulate the coronary arteries (Figure 4). Although this method is not applicable to in vivo imaging and not practical for clinical applications, it is easier to visualize NURD when it is present with this method. A geometrical and feature-based model is used for correction of NURD. Finally, the accumulated torsion induced by the friction on the catheter is measured along the artery path indirectly by the measurement of pullback force using an Instron Micro Tester and is supposed to be an indicator of NURD in OCT imaging.

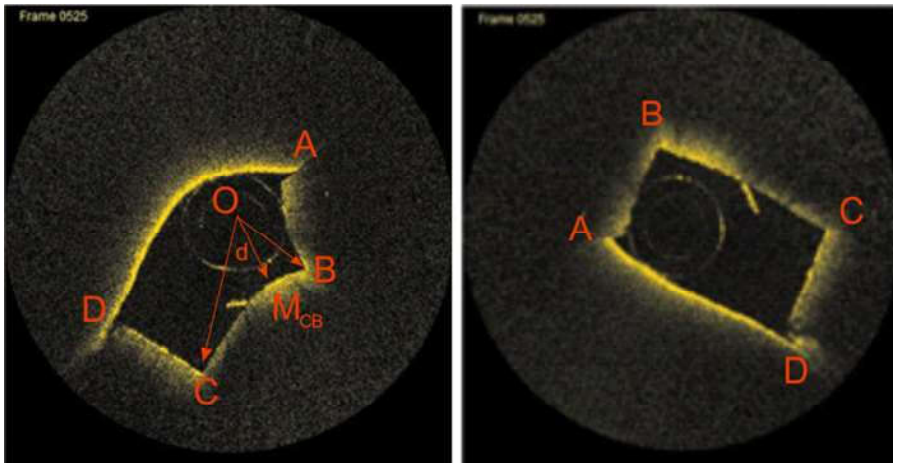

Figure 4: Illustration of NURD occurring in a tortuous path (A) with a rectangular cross-section (B) [19].

A comparison between NURD in OCT and IVUS was conducted in [11]. Two types of vascular phantoms, mild curve (90°) and acute curve (near 180°) were used and the deviation from constant speed was made with 8 wires that were used as fiducial features. Their studies showed occurrence of NURD in OCT is less than half of what happens in IVUS imaging, especially in a

tortuous situation. They concluded that the angular distortion might result in misleading information as in the case of a large angle between the struts which is a predictor of in-stent restenosis. The high lateral-resolving power of OCT is determined as the most important reason in providing precise angle measurements in comparison with IVUS.

Reference [7] presents a technique based on statistical fluctuations of the speckle in the tissue that does not rely on tissue features and can be performed on single frames of data, thereby enabling quantitative determination of the rotational speed of the catheter and real-time image correction. This method, however, requires sufficient azimuthal oversampling and relies on correlation of adjacent a-lines. This method is also prone to physiological movements and is not useful where there is a possibility of abrupt (stick and jump) NURD in the system.

Detecting NURD in micromotor catheters was recently performed in [12] which was based on using spatial markers and was tested in vivo. It used the fixed struts that held the structure of the micromotor as fiducial features and resampled cross-sectional images based on position of mentioned features. Oversampling the data in the longitudinal direction and low time-resolution measure of speed are drawbacks of this method. Also, it emphasizes impracticality of spatial features for tissue movement correction and presence of decorrelation between adjacent frames even in a case of not having a pull-back motion due to the small size of the scanning spot (15micron) and scanning instabilities.

Finally, [6] presents a modified dynamic programming method for correction of NURD in OCT imaging which is the main focus of this article. The proposed method aligns individual lines in a sequence of images and, by finding the least cost path based on similarity of corresponding A-lines of consequent frames, defines the required shift in frame A-lines that can

correct the occurred angular distortion. Although this method still can suffer from presence of abrupt NURD, it can provide a quantitative measure of NURD occurrence in OCT imaging and can be used for real time detection of NURD. The post-processing efforts in this study dealt with providing the codes required for reconstructing the results of this work.

2 MATERIALS AND METHODS

In this section, the theoretical and experimental efforts on NURD correction and feasibility of manufacturing of the probes are described. The theoretical work dealt with finite element simulation of press fitting method and providing the MATLAB coding for an algorithm presented in a former paper on NURD correction. The latter works based on aligning individual A-lines in a sequence of images. It finds a continuous path through a cost matrix that measures the similarity between regions of two frames being aligned.

Experimental works were mainly focused on CT-cap attachment. The importance of this topic is notable because of the effect that it has on the length and axial symmetry of the probe, both of which are highly important factors in the occurrence of NURD. In what follows, each of these main topics is described in detail.

2.1.1 Algorithm for NURD Correction

The angular position of the imaging elements is impossible to be registered in general. As a result, the number of A-lines (about 500 to 2000 here) constituting a movie frame may span a rotation angle that is larger or smaller than the designated 360° that stretches or compresses the angular axis. This continuous NURD makes a part of or the whole frame appear to rotate around its center [6]. Figure 5 is a schematic of changing acquired A-lines to cross-sectional images (A) and a comparison of constant and non-constant angular rotation (B). During a rotation with constant angular speed, A-lines pass through A, B, C and D points in the same time intervals. But if friction on the distal end causes the probe to stick to the sheath wall instantly (stick-slip

situation, resulting in abrupt NURD), it will go from A to B' and then C' and continue to D in the same time intervals. If the friction causes reduction of speed, the same stretching or compression can still happen.

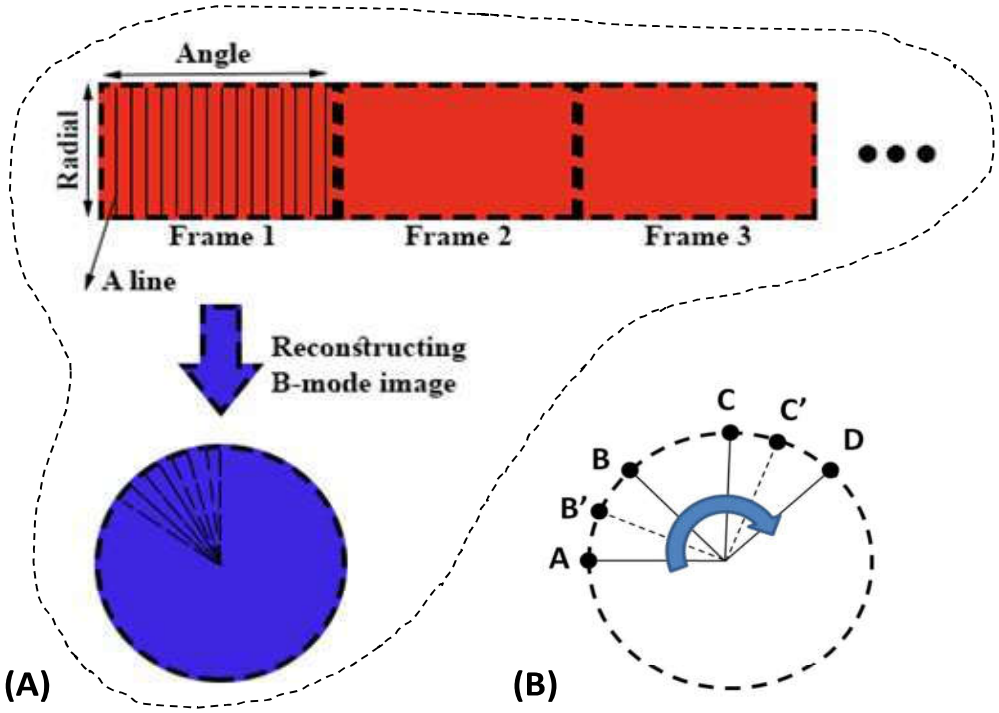

Figure 5: A) Schematic of changing acquired A-lines in polar coordinate to circular cross-sectional images and B) illustration of effect of constant (A, B, C, D) and non-constant (A, B', C', D) angular speed.

In order to correct this angular deviation from the real position, a developed dynamic time warping algorithm, finding a continuous path through a cost matrix that measures the similarity between regions of two frames, is approached. The angular mismatch corresponding to the NURD is corrected based on the obtained path. This code is detecting and correcting the continuous variation in an angular position mismatch. The abrupt NURD can be found by correlation between the speckles in neighboring lines that is out of the scope of this work. The coding is described in detail in the following paragraphs to make it easier to follow, for further developments. Figure 6 shows the first steps of the developed coding.

Read Data:

```
for i=0:N
  im=imread(['Source/nurd/000',int2str(i),'.bmp']);
  frames1(:,:,i+1)=im;
End
```

Define the sufficient width of frames:

```
Width='N';
image_size=size(frames1(:,:,1))
while(Width~='Y')
  u=input('enter required number of pixels in the A_line?','s');
  frames=frames1(1:str2num(u),:,:);
  imu=PolarToIm(im2double(frames(:,:,1)),0,1,1000,1000);
  figure;imshow(imu);title('Sample');
  uu=input('is the depth enough?, Y/N [Y]:','s')
End
```

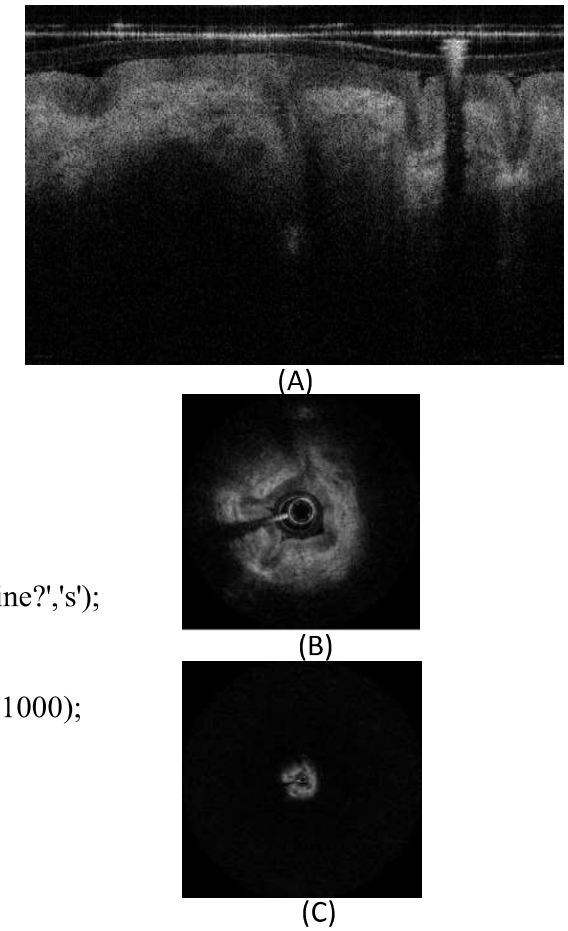

Figure 6: Reading consecutive B- line images and defining the required width. A) A typical B-line image with proper width; B) the constructed cross-section of (A); and C) constructed cross-section with a too large B-line width.

Frames that are considered in the image processing are called in the code. The RGB image of three consequent frames is shown in order to visualize the presence of NURD. The OCT system acquires data as a continuous series of A-lines at a fixed rate. The instrument software groups the data into frames of N_{lines} lines. The typical amount of N_{lines} and number of pixels in each A-line can be 500 and 600, respectively. While the rotation per frame is 360° on average (no long-term net rotation is observed), it is principally unknown for each individual frame.

The procedure used for NURD correction consists of the following six steps:

1) Putting consequent frames after each other so that we have $N_{\text{frames}} \times N_{\text{lines}}$ series of lines Aj ;

2) Providing the cost matrix based on measuring the similarity of corresponding A-lines;

3) Upsampling and downsampling the cost matrix to reduce noise and prevent integer jumps;

4) Dynamic programming solution of the optimal path representing the NURD;

5) Resampling the path to restore the original dimensions of the cost matrix;

6) Reconstructing the frames and correcting the shifts.

An image data radial vector of length N_{pix} corresponding to the smallest angular interval is considered as A-line A_j. The algorithm and all analysis routines were implemented in MATLAB R2015. In the following discussion, j' labels lines within a frame ($j' = 1 \ldots N_{lines}$), while j refers to lines in the concatenated sequence.

Dynamic programming (DP) is the basis of this developed algorithm. It refers to a family of optimization methods that are used for alignment of sequences such as in a database search. This kind of programming method is often used for the purpose of optimization. It solves a complex problem by breaking it down into a collection of simpler subproblems, solving each of those subproblems just once, and storing their solutions. Dynamic time warping (DTW) is a DP technique for measuring similarity between two temporal sequences with same or different speeds. It is used to match two time series by finding the optimal contiguous path using a cost matrix and is a reliable way for matching patterns.

Probe rotation in intravascular imaging is continuous, not only within a frame but also from one frame to the next. This causes the corresponding A-lines to vary slowly and together with continuity of the motion, it makes the NURD problem perfectly fit for treatment with dynamic time warping. However, the approach presented in [6], based on which this coding is performed,

becomes different from DTW methods in that DTW and related methods are developed for matching or alignment of signal curves. However, by warping parts of a periodic image sequence onto itself, a continuous, slowly-varying rotation speed function is recovered. It is possible by using a cost function based on similarity of corresponding A-lines in the frames [6]. Figure 7 shows the polar RGB demonstration of the unprocessed frames (as a better illustration of the angular deviation, A) and the concatenation of frames to $N_{Frames}*N_{Lines}$ series of lines A_j to further be used in development of the cost matrix (B).

Showing 3 consecutive frames in an RGB format:

```
im1=PolarToIm(im2double(frames(:,:,1)),0,1,1000,1000);
 (same for other two frames)
rgb_frame_orig=cat(3,im1,im2,im3);
figure;imshow(rgb_frame_orig);title('Original RGB');
```

Concatenation of acquired B-lines:

```
figure; imshow(Frames); title('frame series original');
```

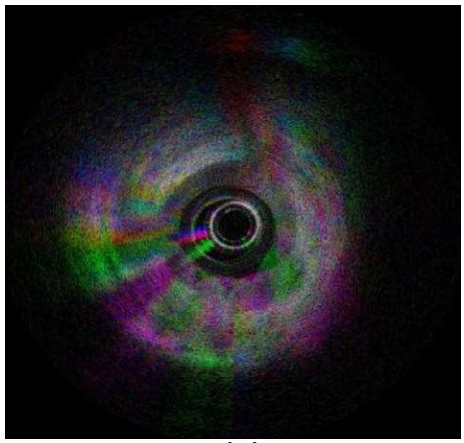

(A)

(B)

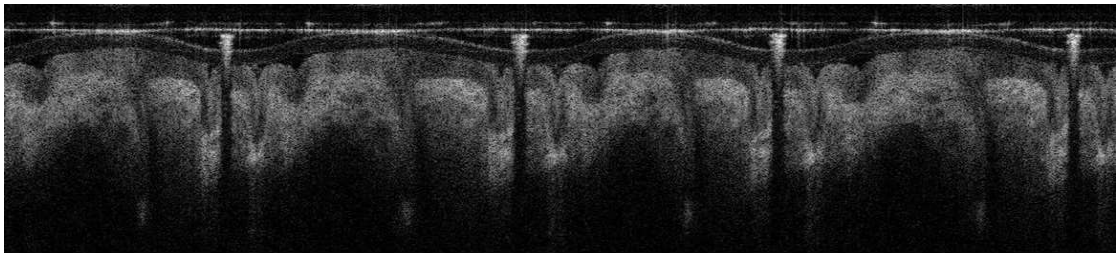

Figure 7: A) Showing the original straight B-lines in a circular RGB cross-section and B) concatenating the frames for the cost matrix.

The cost function is considered to show the degree of similarity between sections of subsequent frames. Depending on the acquired number of A-lines in a frame and point the spread function (PSF) width of the catheter, there might be a lack of intensity correlation in adjacent lines and frames that can cause the cost function based on the unprocessed data to be inherently

noisy. Therefore, in such cases prior to calculating the cost function, convoluting each line with a 1-D Gaussian kernel to remove the sharpest speckle features can be helpful. On the other hand, too much filtering erases some important features and reduces the quality of the alignment. The square root of summation of the difference in pixels intensity between corresponding A-lines (referred to as *L*2 norm of the difference) is suggested as a similarity measure between lines *Aj+k* and $Aj+N_{\text{lines}}$ [6]. The mentioned formula, Eq.1, as well as the cost matrix algorithm is illustrated in Figure 8.

$$C_{k,j} = \sqrt{(A_{j+k} - A_{j+N_{lines}})^2} \qquad [6] \qquad (1)$$

Defined Parameters:

```
n= str2num(input('Enter "n" as the maximum amount of angular deviation: ','s'));
s_value=str2num(input('Enter "s_value" as the amount of subline path precision: ','s'));
m_value=str2num(input('Enter "m_value" as the amount of angle steps over time: ','s'));
Nframes=size(frames,3);
Nlines=size(frames(:,:,1),2);
% n=30;
width=size(frames(:,:,1),1);
```

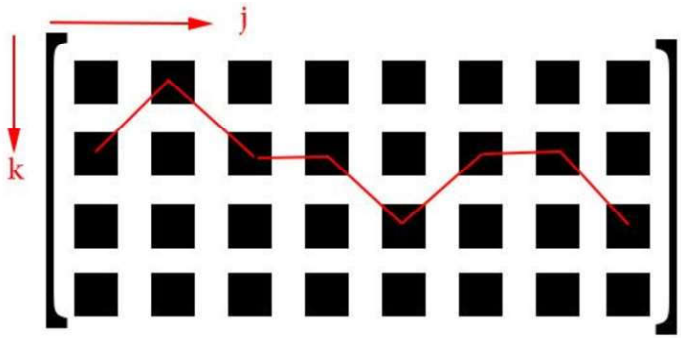

Cost Matrix (C):

```
K=(Nframes-1)*Nlines-n
C=ones(2*n+1,K)*inf;
for j=1:K
   if j>n
      for k=-n:n
         C(k+n+1,j)=sqrt(sum((A(:,j+k)-A(:,j+Nlines)).^2));
      end
   else
      for k=0:n
         C(k+n+1,j)=sqrt(sum((A(:,j+k)-A(:,j+Nlines)).^2));
      end
   end
end
```

Measure of similarity:

$$C_{k,j} = \sqrt{(A_{j+k} - A_{j+N_{\text{lines}}})^2}$$

Figure 8: Defining parameters required for further analysis and calculating the cost matrix.

A better match between A_{lines} is shown when the calculated *Ck,j* is smaller. As a result, the cost matrix elements in a certain column are representative of the similarity of an image line *j* in frame *i* with the lines j - n, . . . , j + n in the previous frame i -1. For more information on this session, refer to reference [6]. The value of "n" has to be larger than the maximum angle deviation between two frames. Considering the maximum angle of deviation as 7 degrees, the value for "n" considering N_{lines}= 500 is calculated by Eq.2 as follows:

$$n = \frac{deviation\ angle(= 7^{\circ})}{360} \times (N_{lines} = 500) = 10 \qquad (2).$$

If the raw cost matrix is used as the basis of analysis, integer matching happens which is not desired when correction of small continuous angular variations is the purpose. Integer shifts can result in accumulating round-off errors. Also, if the cost matrix is not resampled, resulting coarse sampling of integer shifts (in the case of choosing a high "n" value), in combination with the recursive application of the shifts at the final steps of processing, results in a marked deterioration of the algorithm for longer movies. Non-integer shifts are a good remedy for this issue.

The cost function is resampled in the following manner to provide the step constraint for suppression of unrealistic jumps and remove the noise. The matrix *Ck,j* is stretched by a factor *s_value* in the vertical *k*-direction (to get subline path precision) and compressed by a factor *m_value* along *j* (reducing noise and further constraining the angle steps over time). A path through this matrix takes steps of size 1*/s_value* in *k* and of size *m_value* in j directions. Tuning *m_value* and *s_value* allows one to match the sampling of *C* to the dynamics of the problem, particularly the maximum angular deviation. C^R has dimensions *K/m_value* by 2 × *s_value* × *n* + 1. This cost matrix is used as input to the path optimization algorithm.

A continuous horizontal path is determined from left to right in the resampled cost matrix C which is considered as the optimal path, representing the NURD correction (Figure 9). The path continuity is constrained in a way that maximum change in rows from one column to the next is only one row. The costs of all elements in a path define its cost. The path with the lowest total cost is considered as the most optimum path. By knowing the total cost ($g_{k,j\text{-}1}$) of the optimal partial paths up to each element of column j - 1 of the matrix, optimal costs ($g_{k,j}$) for all elements of the next column (j) is calculated by Eq.3:

$$g_{k,j} = C_{k,j} + min_{l=k-1,k,k+1}\{g_{l,j-1}\} \quad [6] \quad (3).$$

Considering the cumulative cost for column 1 as $g_1 = C_1$, the cumulative cost for each of the following columns is calculated, and at the same time the track of the optimal predecessor of each element is recorded. The element with the minimal value in the last column will be the end of the optimal path.

Up sample and Down sample C

```
C_old=C;
C=C_old;
[mm,nn]=size(C);
C=C_old(:,1:10:end);
C=interp1(s_value:s_value:mm*s_value,C,1:mm*s_value,'spline');
```

Cost of possible paths (g):

(g1=C1)

$$g_{k,j} = C_{k,j} + \min_{\ell=k-1,k,k+1} \{g_{\ell,j-1}\}$$

Cost of Possible Paths:

```
g=zeros(size(C));
g(:,1)=C(:,1);
track=ones(size(C))*inf;
for j=4:size(C,2)
for k=1:size(C,1)
```

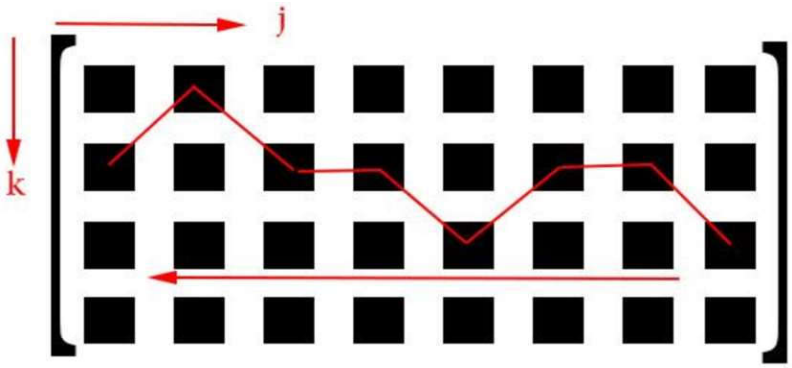


```
   if k==1
      g(k,j)=C(k,j)+min([g(k,j-1),g(k+1,j-1)]);
      qq=find([inf,g(k,j-1),g(k+1,j-1)]==min([inf,g(k,j-1),g(k+1,j-1)]));
      track(k,j)=qq(1);

   elseif k==size(C,1)
      g(k,j)=C(k,j)+min([g(k-1,j-1),g(k,j-1)]);
      qq=find([g(k-1,j-1),g(k,j-1),inf]==min([g(k-1,j-1),g(k,j-1),inf]));
      track(k,j)=qq(1);
   else
      g(k,j)=C(k,j)+min([g(k-1,j-1),g(k,j-1),g(k+1,j-1)]);
      qq=find([g(k-1,j-1),g(k,j-1),g(k+1,j-1)]==min([g(k-1,j-1),g(k,j-1),g(k+1,j-1)]));
      track(k,j)=qq(1);
   end
 end
end
```

Figure 9: Upsampling C in the vertical (k) direction and downsampling it in the horizontal (j) direction.

By tracking back, considering the archived steps [k - 1, k, k + 1], the full path can be constructed. The achieved continuous path P represents the slowly varying angle deviation induced by the slow speed variations. The coding for this section is presented in the following lines:

Re-track Path

```
optimal_path=ones(size(C,2),1)*(n+1)*10;

for i=size(C,2):-1:4
  min_row=find(g(:,i)==min(g(:,i)));
  optimal_path(i)=track(min_row,i)+min_row-2;
end
optimal_p=cat(1,optimal_path,ones(3,1)*(n+1)*10);
optimal_path1=floor(interp1(1:10:size(optimal_p,1)*10-9, optimal_p,1:1:size(optimal_p,1)*10,'cul

Po=optimal_path1-(n+1)*10;
```

Before the shifts are applied, the constructed path resulting from the optimization is upsampled to have the original dimension of the cost matrix (with length K). P defines the amount of shift for each A-line. Based on the calculated P, frames were reconstructed (Figure 10).

Aligning the A-lines might shift the position of the lines in frame $i-1$ that are used for correcting frame i. Thus, we need to correct for these shifts: in order to find Pi, which is correcting frame i, the shifts in the aligned positions in frame $i-1$ should be calculated first by Eq.4:

$$P^{a}_{ij'} = P(j' + (i-1)N_{lines} + P^{a}_{i-1\ j'} \quad [6] \qquad (4).$$

The first frame is assumed to have a zero shift ($P^{a}_{ij'} = 0$). The optimal path illustrates the angle deviation between consecutive frames. Therefore, we can obtain the correction P for the deviation over a sequence up to frame i by accumulating the deviations P^{a} up to that point as is presented in Eq.5:

$$P'_{ij'} = \sum_{q=1}^{i} P^{a}_{qj'} \qquad [6] \qquad (5).$$

Re-Construct ion of Frames:

```
A_new=zeros(width,K);
As=interp1(1:10:size(A,2)*10,A',1:1:size(A,2)*10,'cubic')';

for i=2:K
   A_new(:,i)=As(:,i*10+Po(i));
end
figure;imshow(A_new(:,1:2*Nlines));

 cf1=A_new(:,1:Nlines);
cfr1=PolarToIm(im2double(cf1),0,1,1000,1000);
 cf2=A_new(:,Nlines+1:2*Nlines);
cfr2=PolarToIm(im2double(cf2),0,1,1000,1000);
rgb_frame=cat(3,cfr1,cfr2,zeros(size(cfr1)));
figure;imshow(rgb_frame);
```

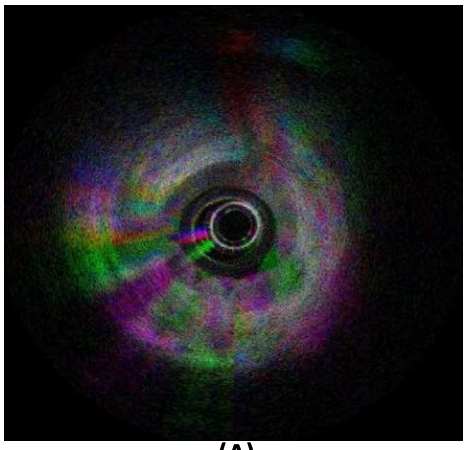

(A)

Correction of Shifts:

```
P=floor(Po/10);
Pa=zeros(Nframes-2,Nlines);
A_shift=A_new(:,1:2*Nlines);
for i=2:Nframes-2
for jp=1:Nlines
j=jp+(i-1)*Nlines;
Pa(i,jp)=P(j+Pa(i-1,jp));
A_shift(:,j)=A_new(:,j-Pa(i,jp));
end
end
```

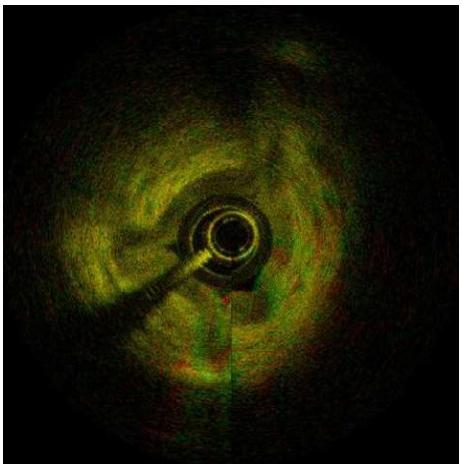

(B)

Figure 10: Reconstruction of frames based on the optimum path found.

The fact that $P'_{ij'}$ is generally non-integer suggests nearest neighbor interpolation of image A-lines for performing the final alignment. The proper data transfer between frames is assured by the accumulated shift being based on the continuous sequence.

Currently, it is not feasible to provide a reference NURD free frame to compare it with the acquired frames and find the NURD. The standard deviation of the aligned frames, normalized to the mean aligned frame is suggested to be used as a measure for the quality of the alignment and

performance of the algorithm, Eq.6. Smaller standard deviation is an indication of better alignment. This measure and the corresponding code is shown in the following lines where $\tilde{\sigma}(a_{j'p})$, Eq.7, is the standard deviation of the mean value of pixel j'_p in the aligned sequence, $\bar{a}_{j'p} = (\frac{1}{N_{frames}}) \sum_i a_{ij'p}$. N_{tis} is the number of pixels in the "tissue," included in the summation. Uncorrelated speckles are sampled in different frames, so perfect alignment minimizes the standard deviation, but not to zero.

$$\langle \sigma(a) \rangle = (N_{\text{tis}})^{-1} \sum_{j',p \notin \text{lumen}} \tilde{\sigma}\,(a_{j'p}) \qquad [6] \qquad (6)$$

$$\tilde{\sigma}(a_{j'p}) = \sigma(a_{j'p})/\bar{a}_{j'p}, \sigma\,(a_{j'p}) \qquad [6] \qquad (7)$$

The following lines represent coding for calculating the standard deviation:

```
frames=cat(3,im1,im2,im3,im4);
[M,N,O]=size(frames);
data=im2double(reshape(frames,M*N,O));
std_mat=std(data');
mean_mat=mean(data')+.0001;
norm_std_mat=std_mat./mean_mat;
mean_norm_std=sum(norm_std_mat)/(M*N);
val score=mean norm std.
```

Another part of theoretical work dealt with finite element analysis of the mechanical press fitting process as is described in the following session.

2.1.2 Finite element analysis of the press fitting process

Press fitting method is a promising process for attachment of cap and TC as discussed further in the *Results and discussion* section. Two different configurations, fixed two-jaw (FTJ) and adjustable six-jaw (ASJ) forming, were considered and investigated through simulations. These configurations are illustrated in Figure 11. Arrows are an indication of the applied external forces on the specimen. "Fixed" and "adjustable" are describing the nature of forming equipment.

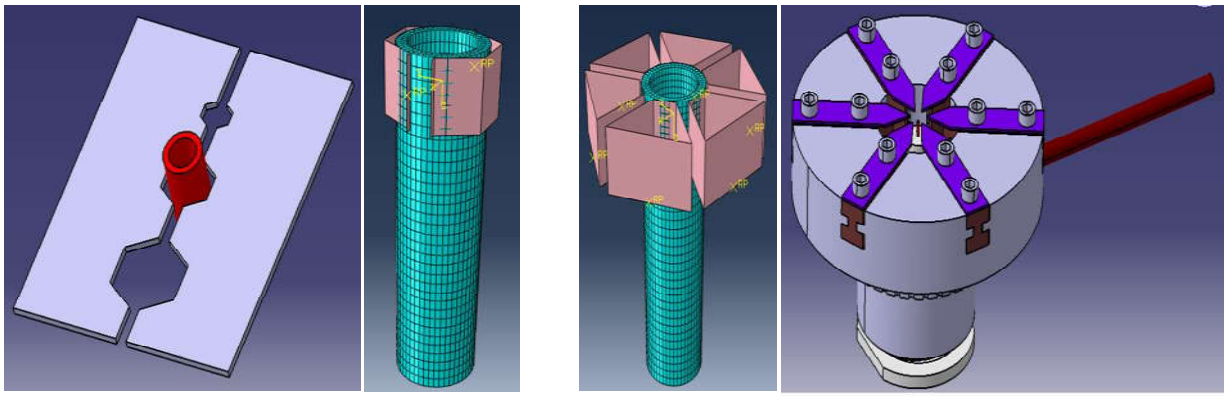

Figure 11: Two different press fitting configurations considered for finite element simulations: (A) fixed two-jaw (FTJ) and (B) adjustable six-jaw (ASJ) forming methods.

Finite element simulations using ABQUS 6.14 software were conducted to monitor the stress distribution and uniformity of the cap deformation in each of these two configurations. Table 1 shows the defined parameters for the parts in the current simulation.

Table 1: Parts' features in the current finite element simulation

Model	Part Name	Type	Base feature	Modeling space
Adjustable six jaw forming	Adjustable Jaw	Discrete rigid	Shell, extrusion	3D
	Cap	Deformable	Solid, extrusion	3D
Fixed two jaw forming	Fixed jaw	Discrete rigid	Shell, extrusion	3D
	Cap	Deformable	Solid, extrusion	3D

Elastic-plastic properties of stainless steel (SSt) 304 material, as a common steel for medical applications, was used in simulations. Figure 12 shows the dimension of the specimen as well as the elastic-plastic mechanical properties of SSt304 based on Holloman-Ludwik equation (Eq.8, [20]):

$$\sigma = (K = 1.393 \times 10^9) \times (\varepsilon_{total} - \varepsilon_{elastic})^{(n=0.4062)} \quad [20] \qquad (8)$$

in which σ is the stress, K is the strength coefficient, ε is the strain and n is the strain hardening exponent.

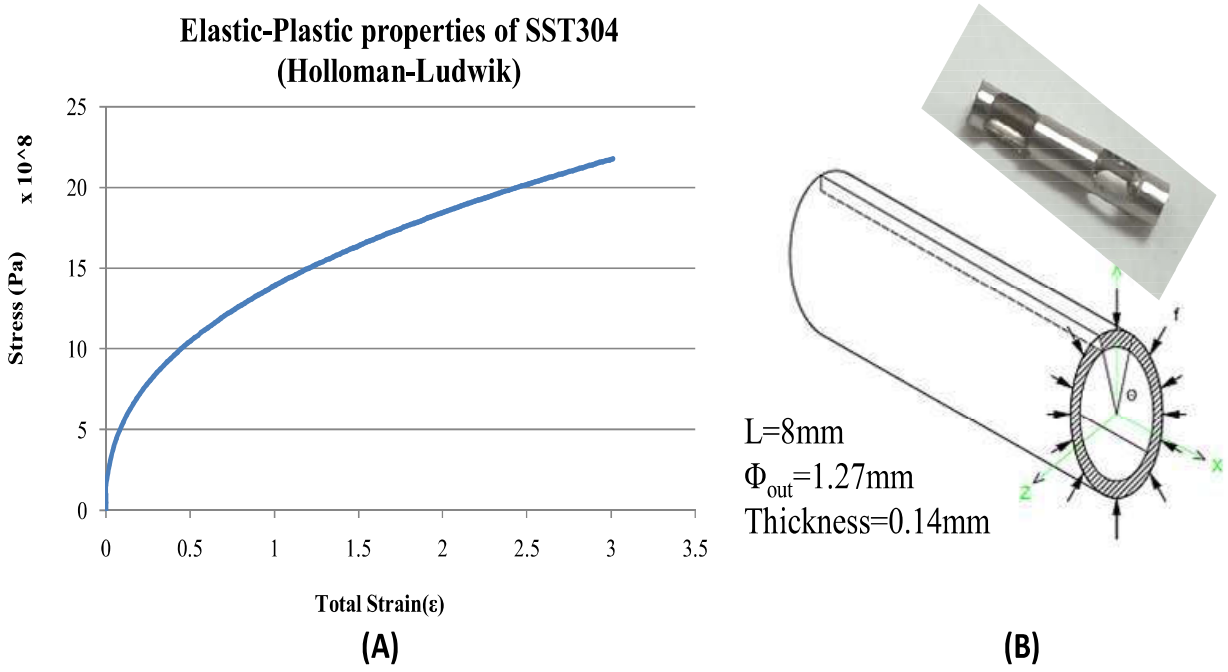

Figure 12: (A) Elastic-plastic material properties for stainless steel 304 and B) deformable part dimensions used in finite element simulations.

Simulations were conducted in ABAQUS/Explicit environment. Table 2 is a representation of important input data in different modules of the software for the current simulations.

Table 2: Input data used in different modules of software

Section type	Mesh type	friction	Step time	Step type	Amplitude
Solid, Homogeneous	Hex-dominated, Structured	0.6	0.01 sec	Dynamic, explicit	Smooth

2.1.3 Experimental model for investigating the presence of NURD

A model for mimicking the tortuous path of a blood vessel was made and is illustrated in Figure 13-A for future work on investigating the presence of NURD and its type for the current OCT system. The bulk material was chosen to be urethane. Since tracking the fiducial features of the model was the main goal, scatterers were not used in the current model. Apart from its transparency and elastic behavior, the viscosity of urethane during the mold pouring is almost ten times less than silicon which helps it to go into detailed parts of the mold and mimic sub-millimeter features. This is important for the current model in that it should sufficiently fill the space between wires and between wires and the tube. However, the cure time of 24 hours is a drawback in comparison with half an hour for silicon.

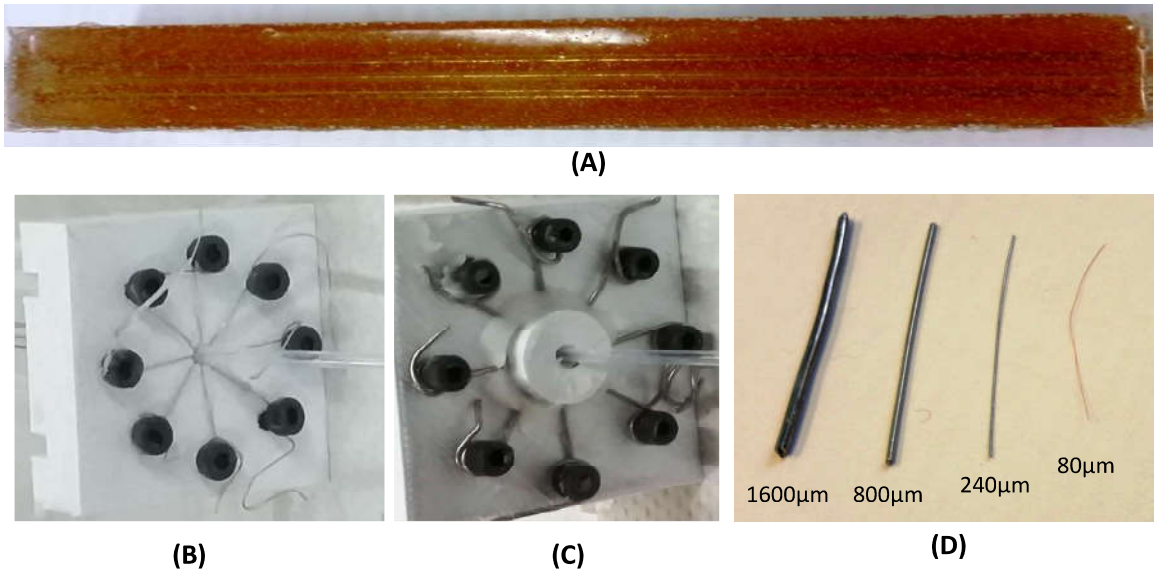

Figure 13: (A) Urethane model for investigating the presence of NURD for future studies, B) & C) 240µm and 800µm wires put under tension using screws, and D) 4 different wires considered for making the model.

Four different wire thicknesses (80µm and 240µm copper and 800µm and 1600µm soldering wires, Figure 13- D) were considered for making the model. 800µm wires had significant signals (unlike 240µm wires) and were easy to keep straight with a reasonable amount of tension (unlike 1600µm wires). Thus, eight 700 micron diameter soldering wires were chosen for the final model and were placed at 45 degrees around the blood vessel mimicking tube to further detect any NURD based on a comparison between angular distance of wires in cross-sectional images and the real angles in the model (45 degrees). Soldering wires are flexible enough to become straight when tension is applied to them using screws in the mold (Figure13-B&C) and also have very low resistance against bending in the model when the model is extremely bent. The designed mold is shown in Figure 14.

Figure 14: Designed mold for NURD investigation model.

The blood vessel mimicking tubes chosen were 2mm and 4.7 mm diameter. The rationale for 2mm diameter was the more precise movement of the probe inside it and the closer distance of

the wires from the probe which helps better detection. The 4.7mm tube was chosen to be close to the extreme size of human coronary arteries[1].

Finally, holders of different curvature (100 and 150mm diameter) with signs indicating the angular bending were designed and 3D printed (Figure 15-A) to further investigate the effects of bend radius and angle on the presence of NURD. This artifact is not obvious in curvatures with a radius larger than 105mm; however, it will be obvious when the curvature becomes less than 75 mm in radius [11, 19].

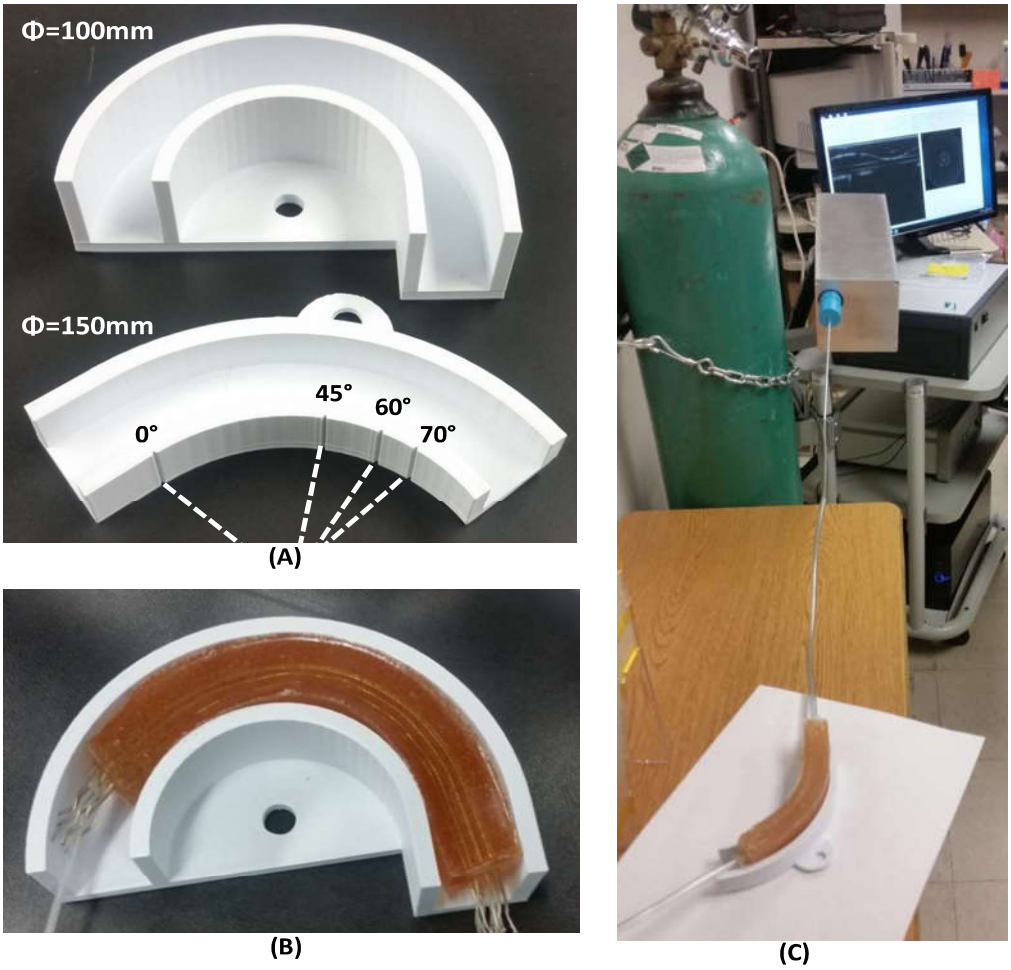

Figure 15: A) Designed NURD model with different bending radius and angular signs for checking the effect of bending angle, B) holding model in a 100mm diameter holder, and C) preparing the model for OCT imaging.

[1] http://circ.ahajournals.org/content/86/1/232

2.2 Manufacturing of probes

Here, the efforts on making probes were mainly focused on optimizing the connection of cap to the torque coil. It is of high importance especially due to effects that it has on the rigid length of the probe tip and its axial symmetry. These two latter properties can highly affect the quality of images and the occurrence of NURD. The more rigid length of the distal end of the probe can cause more friction and inconstant angular speed while its axial out-of-symmetry can again cause more friction due to centrifugal forces resulting in higher normal pressure between sheath and probe at the distal tip.

2.2.1 Torque Coil-cap (TC-cap) attachment

Four different methods are considered in this section. Features that were considered in evaluation of each process were: need for skilled technicians, scalability of the manufacturing process, strength of the joint, axial symmetry of the connection, resulting rigid length of the probe tip and amount of control over it, and, finally, environmental effects of the process.

2.2.1.1 Gluing and soldering

A common soldering process with 95%Sn lead free solder, solder paste (SMD291SNL250T3), and a bath of solder were tested to check the feasibility of this process (Figure 16). Epoxy glue was not tested due to practical drawbacks discussed in the *Results and discussion* session.

Designing a fixture to keep the cap and torque coil in the exact same place each time in these two processes in order to make them repeatable and reliable is difficult mainly because the fixture will be smeared into the solder or glue, and this is a problem, especially in sub millimeter dimensions.

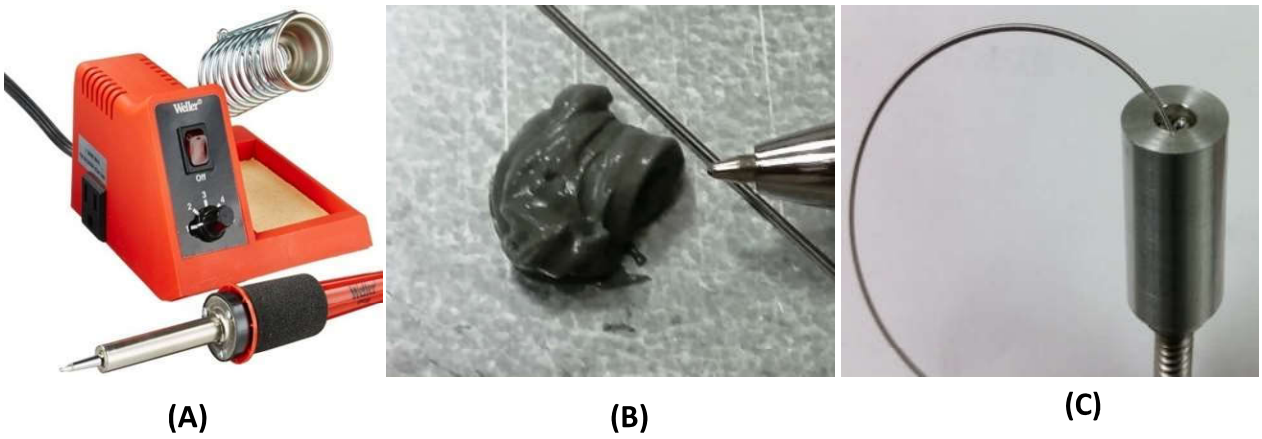

Figure 16: Soldering using A) common soldering tool, B) solder paste, and C) bath of solder for improving wettability.

2.2.1.2 Electrochemical processes

Two electrochemical processes were approached in these series of experiments. Electrochemical etching was performed on the tip of the TC to provide a cylindrically fine end which is critical in assembling the TC and cap. Figure 17 shows a typical electrochemical etching process in which TC is the anode electrode and is corroded.

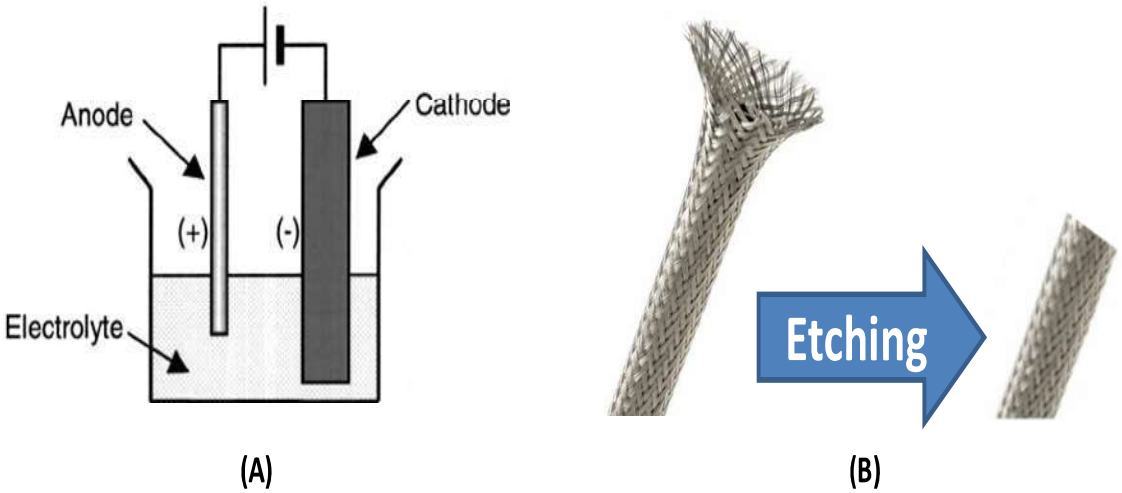

Figure 17: A) Schematic of electrochemical etching[2] in which TC is the anode and will be corroded away and B) illustration of effect of electrochemical etching on TC end.

[2] http://dx.doi.org/10.1063/1.1355262

Two different acidity levels for vinegar [7% (red) and 5% (white)] were used. The setup used for the electrochemical etching process is shown in Figure 18.

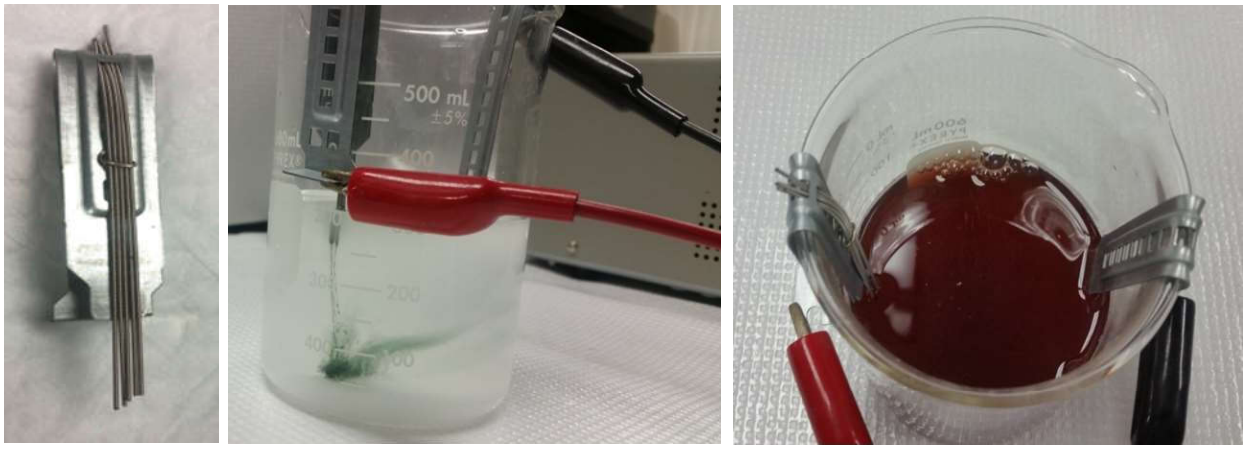

Figure 18: A) TC holder, B) white vinegar (5%) and red vinegar (7%) used in experiments.

Electrochemical deposition also has previously shown success in attaching different conductive components [21, 22]. It was considered as a potential method for connecting the TC to the cap. A schematic of the process is shown in Figure 19.

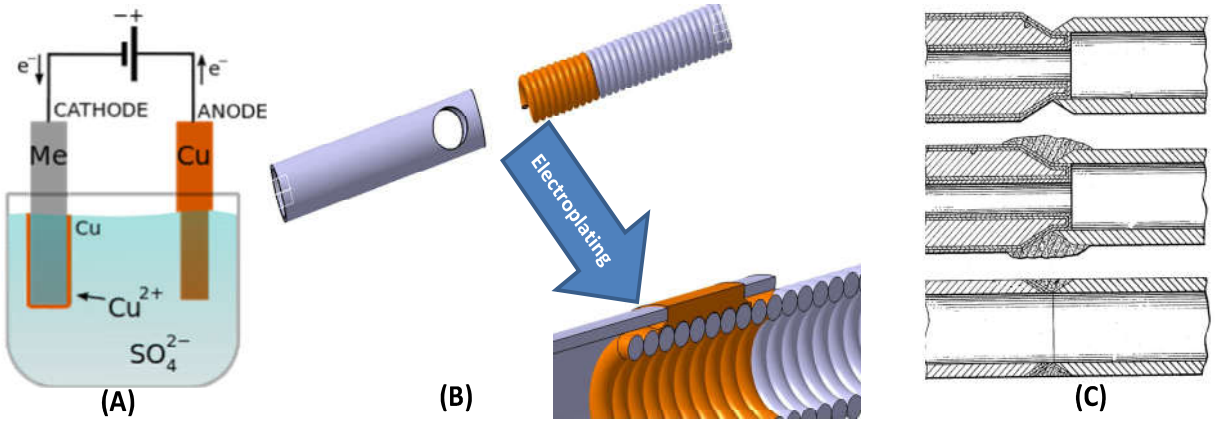

Figure 19: A) Schematic of electroplating process[3] (here copper plating), B) schematic of TC-cap joining in this process, and C) previous work on similar and dissimilar metal pipe joining with this process [21].

[3] https://www.comsol.com/blogs/electroplating-u-s-mint-makes-penny/

Nickel (Figure 20-A) and copper (Figure 20-B) plating were considered for TC-cap attachment. Since the simplicity and feasibility of the process was important in choosing between different methods, copper plating was performed as the first choice. Nickel plating was then performed due to lack of joint strength in copper plating. Heat shrink tubes were chosen both as cover for places that should not be coated and for fixing the TC and cap in position (Figure 20-D). Details of the experiment chemicals and variables are shown in Table 3 [23].

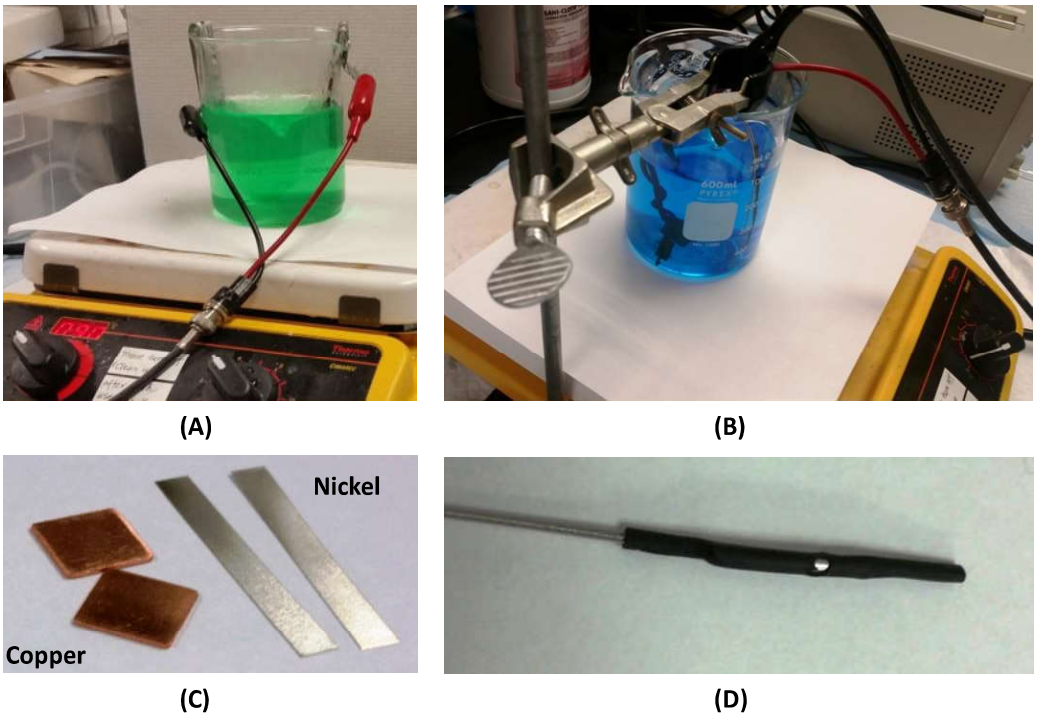

Figure 20: A) Nickel plating, B) copper plating, C) electrodes, and D) using heat shrink tubes for covering areas that should not be coated.

Table 3: Chemicals and setup for the electrochemical experiments

Process	Anode	Cathode	Electrolyte	Temperature	Duration
Electrochemical etching	TC	Steel plate	Vinegar (5% & 7%) saturated with salt	Room Temperature	7 minutes
Copper plating	Copper plate	TC	10% cupric sulfate	60°C	30 minutes
Nickel plating	Nickel plate	TC	9% nickel ammonium sulfate	90°C	60 minutes

2.2.1.3 Mechanical press fitting

The cross-sectional shape of the joint area is preferred to be hexagonal due to its axial uniformity and ease of manufacture. Two methods are approachable for making the press fitting equipment. However, simulations suggested the adjustable six jaw configuration promising. Thus, required parts were designed with CAD software (CATIA R20) and manufactured as shown in Figure 21-A. This equipment allows for making probes of different sizes in the same setup. 1095 spring steel blades of 0.5 mm and 1 mm were used as forming jaws in the adjustable six jaw setup and laser cut Plexiglas was used as a pattern for making wholes and cuts (Figure 21-B). Also, in order to make parts as precise as possible, holders were made to fix parts during machining as shown in Figures 21-C&D.

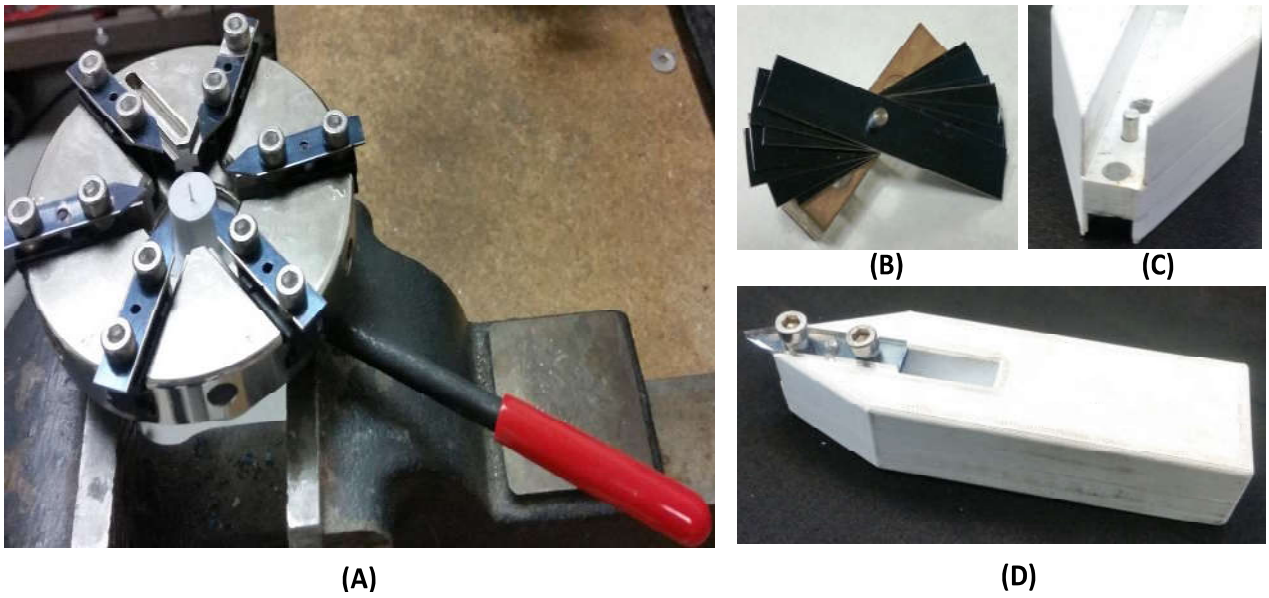

Figure 21: A) Designed equipment, B) laser cut Plexiglas used as a pattern for machining of plates, C) using pins for precise positioning of blades, D) made holder for machining of blades.

3 RESULTS AND DISCUSSIONS

3.1 NURD correction results:

The provided NURD correction MATLAB coding contains a figurative output and a quantitative output as a way to measure the effect of post-processing. As shown in Figure 22-A, only the part that is shown in the dashed line is experiencing a large distortion which is well corrected as illustrated in Figure 22-B. As the "n" (indicating the allowed distortion of the image) increases, a couple of sharp lines start to appear in the image which is shown in Figure 22-B. However, these artifacts belong to the consideration of an excessive NURD more than 6 degrees which is rare in the case of gradual distortion of the image resulting from continuous NURD [6].

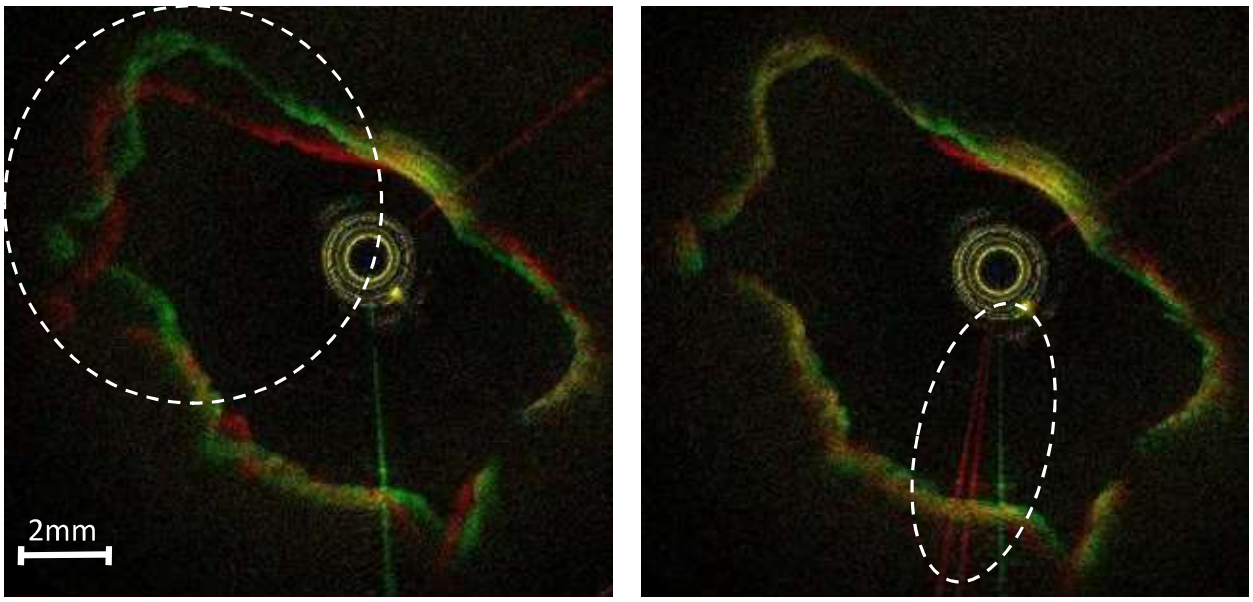

Figure 22: A) NURD shown in two consecutive frames (red and green) by the dashed line for human subject upper airway and B) corrected distortion and radial artifacts (in dashed line) due to too large allowed distortion in coding.

Another artifact that can happen during the processing is the repetition of an A-line in a portion of the image as a result of integer jumps between A-lines. This artifact is illustrated in Figure 23-A. In order to come over this issue, the interpolation and upsampling of the cost matrix is suggested in [6].

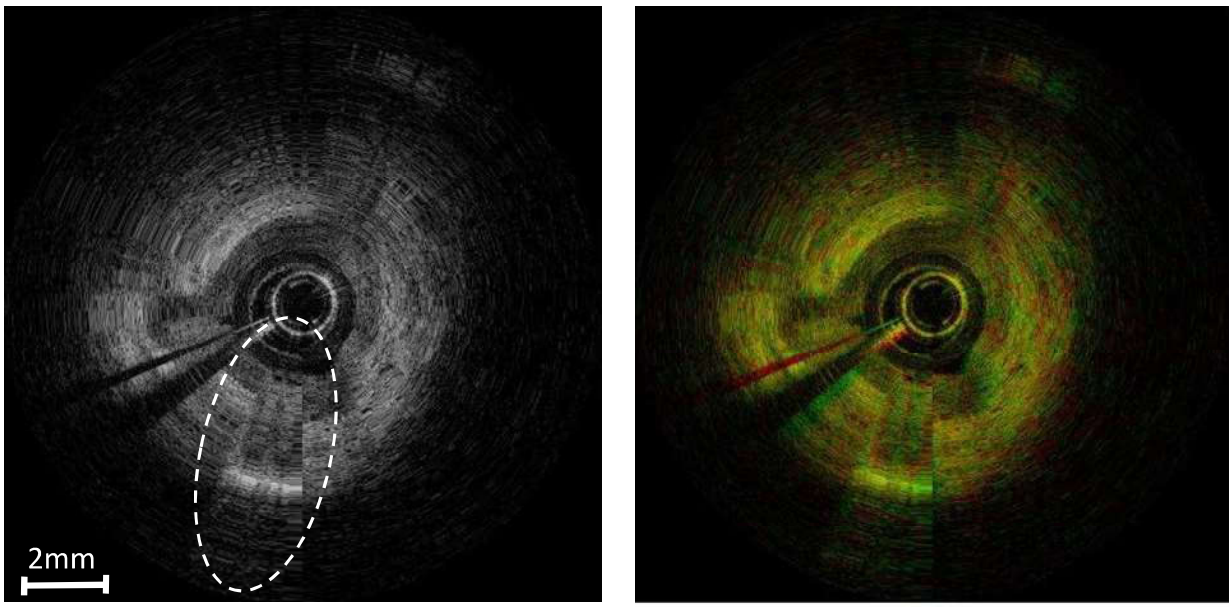

Figure 23: A) Repetition of an A-line in a portion of the image as a result of integer jumps and B) the same frame in an RGB image with the previous frame.

A great advantage of this algorithm is fast processing the data. For example, quantitative assessment of original and processed images is performed in less than 35 seconds for four frames and the figurative outputs are provided in less than 90 seconds for the same number of frames. It facilitates further development of the method and makes it easy to use it at the same time as other algorithms due to an insignificant load on the processing equipment.

Due to the dynamic programming basis of this algorithm and correction of distortion based on previous available data, the method is prone to accumulation of errors, especially when the number of processed frames increases (more than 10 in case of severe NURD). Thus, it is

suggested that this algorithm be a tool for correction of NURD in a selective portion of the frames which is found to have NURD, either by the quantitative method in this paper or another method.

Three different sets of data containing NURD were tested with the current algorithm and the results well illustrate the effect of NURD correction on the processed data (Figure 24). For the current algorithm, the output is defined to be the second frame which is reconstructed and then shift corrected. This frame is shown in an RGB figure with the first (reference) frame to demonstrate the effect of corrections.

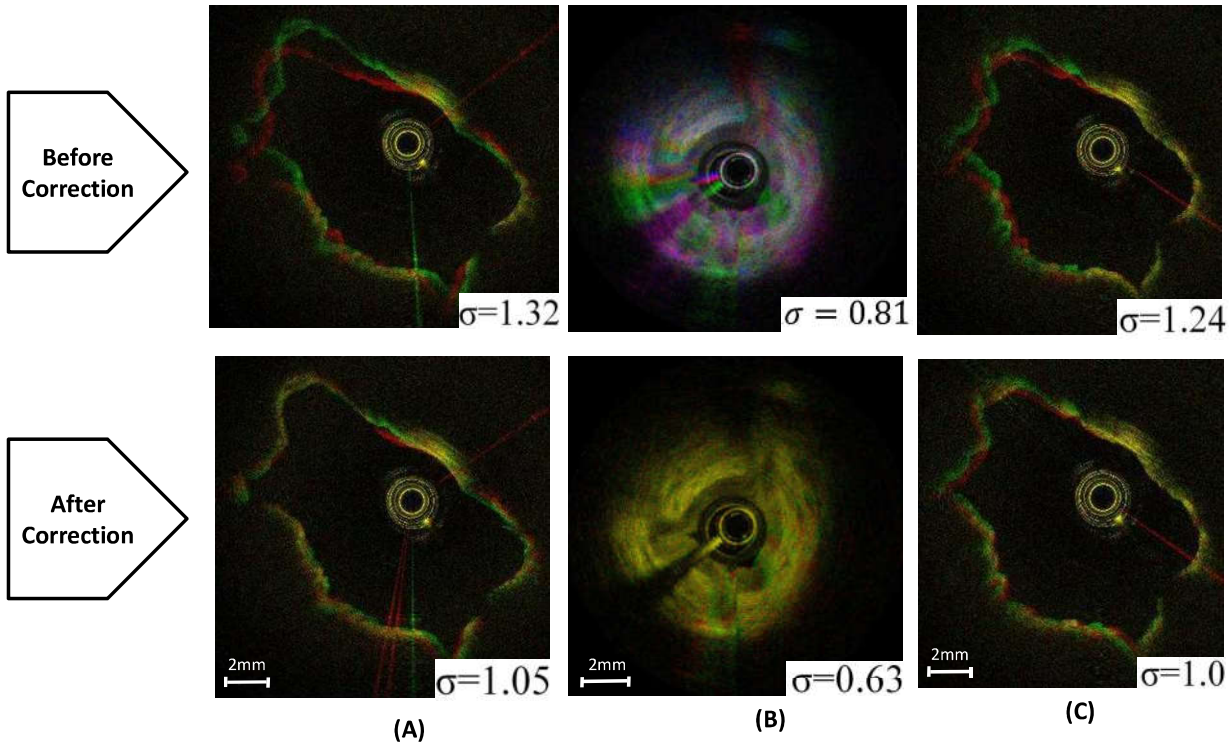

Figure 24: final figurative and quantitative results of NURD correction algorithm for a human subject upper airway.

Since the lumen area is not eliminated from the processed data, the amount of standard deviation is large for these sets of data which is consistent with the reference paper ([6]). The experimental

model for detailed investigation of the presence of NURD and its type in the current OCT system has been developed and will be a purpose for future study. An important feature of this model is the possibility of testing different bending radius and angles with the same model and no need in making different models for different bend radiuses. Having the same model for different conditions makes it more accurate to compare acquired frames, since all images belong to the certain geometry with fixed spatial features.

3.2 TC-cap attachment

3.2.1 Importance of the TC-cap attachment

Axial symmetry and length of the rigid part of the probe tip are important parameters in the presence of NURD. The more tortuous a path, the more NURD will be present in the acquired images. If we consider the critical bending radius of the tortuous path as a measure for the presence of NURD, the larger critical bending radius will be a sign for the presence of more severe NURD. Important dimensions are demonstrated in Figure 25. Based on the relation presented in [19] for the critical bending radius, Eq.9, the importance of the cap-sheath gap (d_t - d_p) and rigid length (L) of the probe can be depicted as in Figure 26 and Figure 27, respectively. The critical bending radius is calculated in the following manner:

$$R = \frac{d_t - d_p}{2} + \frac{L^2}{8(d_t - d_p)} \qquad [19] \qquad (9)$$

where d_t is the inside diameter of the sheath, d_p is the probe tip diameter, L is the length of the rigid part of the probe tip and R is the critical bending radius.

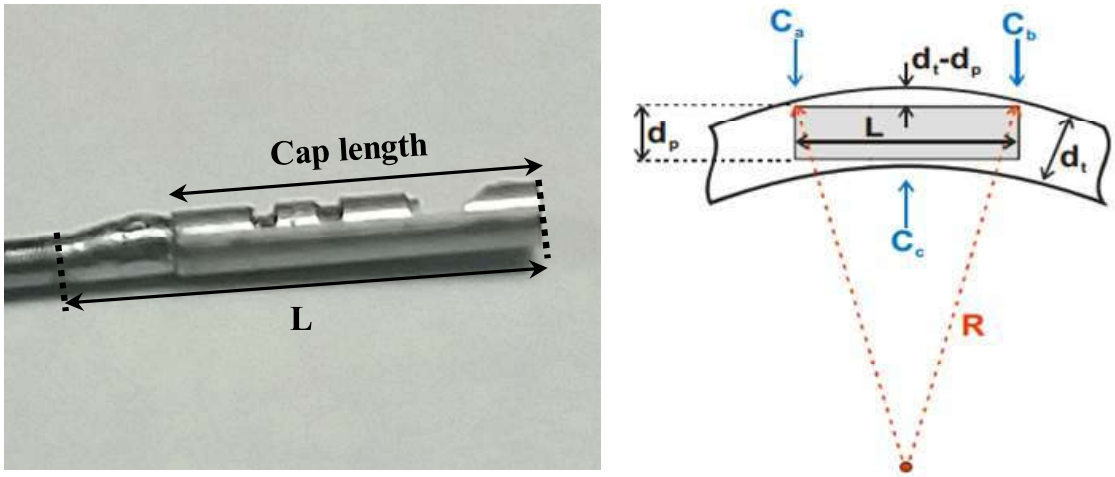

Figure 25: A) Rigid length of the probe tip (L) shown on the actual probe and B) a schematic of dimensions including critical bend radius (R) [19].

By reducing the cap-sheath gap, the critical bending radius increases, especially for $d_t - d_p < 0.2$. The change of the rigid length of the probe tip from 6mm to 8mm, shown in Figure 26, increases the critical bending radius and thus the possibility of the presence of NURD by twofold. It shows the importance of keeping this region as short as possible.

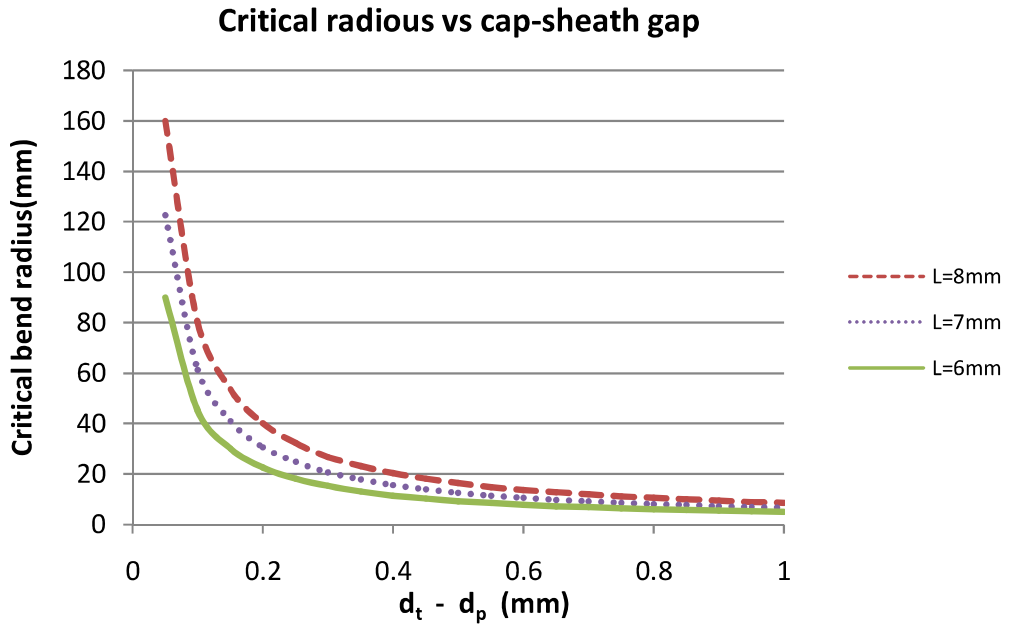

Figure 26: Effect of cap sheath gap change on critical bending radius for three different constant rigid length of the probe tip.

Rigid length (L) of the probe tip is another important parameter as is shown in Figure 27. The change in length can drastically change the critical bending radius and raise the possibility of NURD occurrence. This effect becomes more and more severe when the cap-sheath gap reduces.

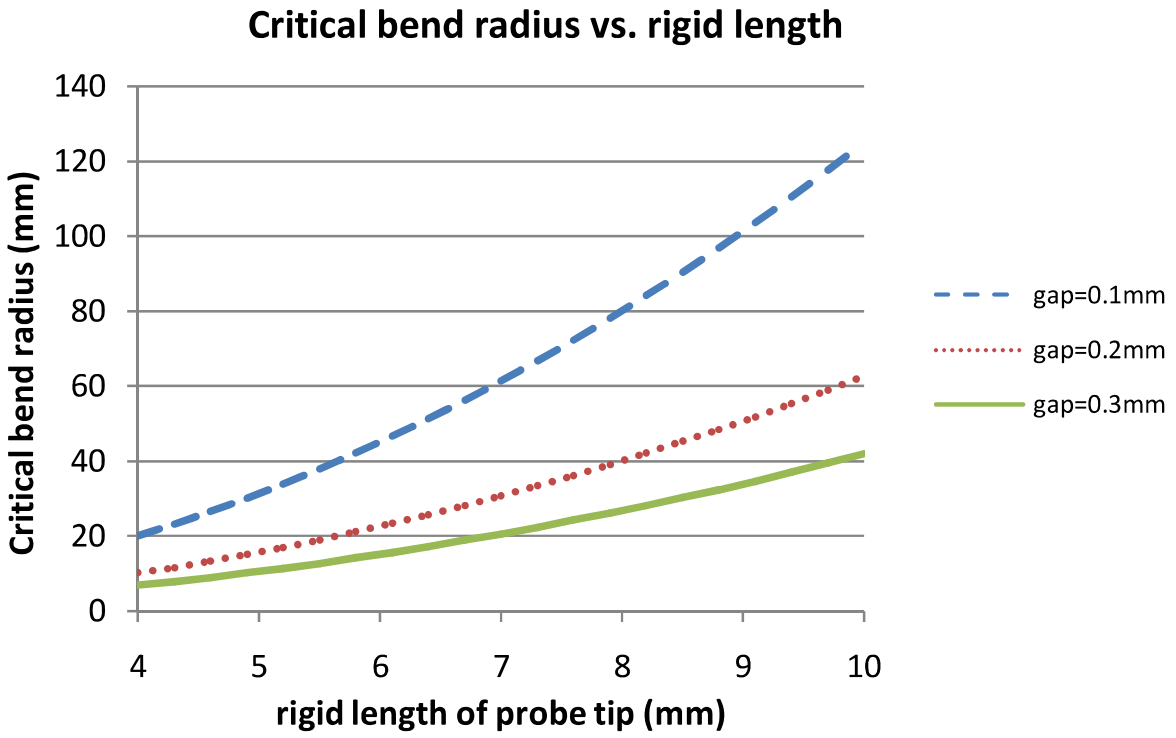

Figure 27: effect of the rigid length of the probe tip on critical bending radius for three different constant cap-sheath gaps.

The gap between TC and cap also can cause a twofold drawback. First, it can reduce the cap-sheath gap when the cap and TC are not concentric. This issue is well illustrated in Figure 28. In this figure, Φ1 is the cap radius and Φ2 is the actual radius in which the cap rotates; a case of perfect cap-TC parallelism. This results in an increase in the critical bend radius of NURD due to reducing the cap-sheath gap. This is not avoidable in gluing, soldering and even electroplating which will be a drawback for these processes.

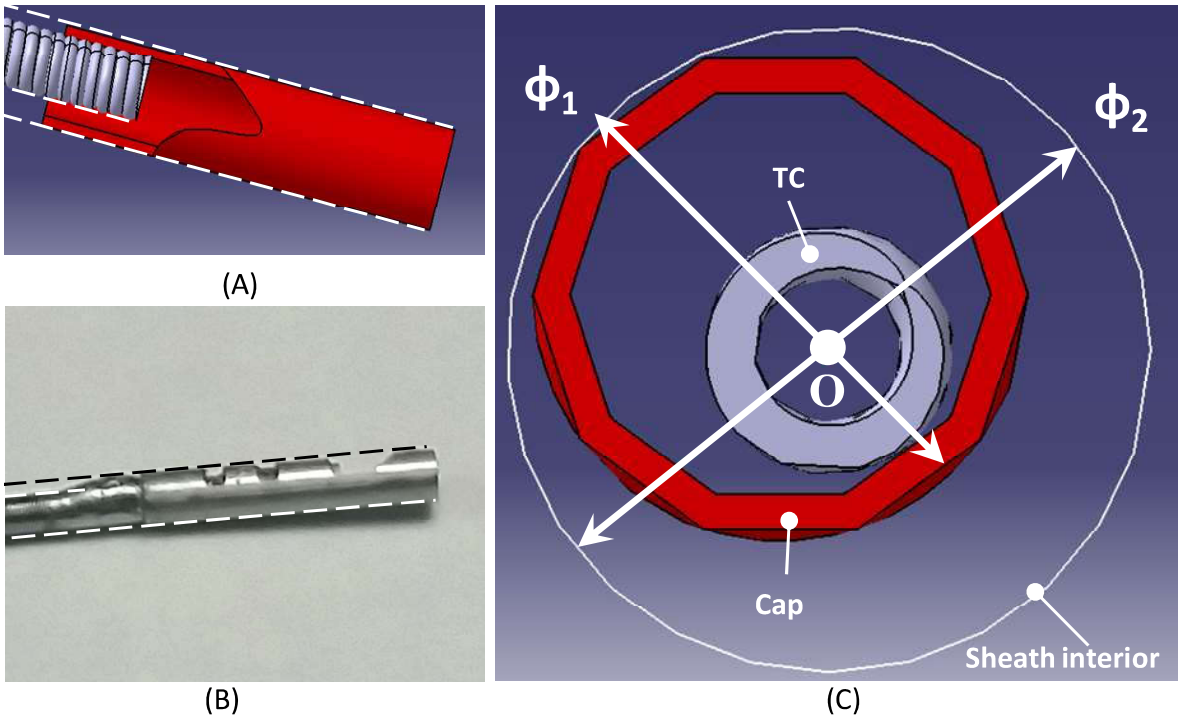

Figure 28: A) Cap and TC are not concentric, B) the problem in actual probe, and C) exaggerated nominal (Φ_1) and effective (Φ_2) diameter of the cap.

Second, it can cause out-of-parallelism error as shown in Figure 29. This out of parallelism will have a worse effect than being out of center since cap length increases the radius that the probe tip moves in each rotation and, thus, reduces the distance between sheath and probe (cap-sheath gap reduction).

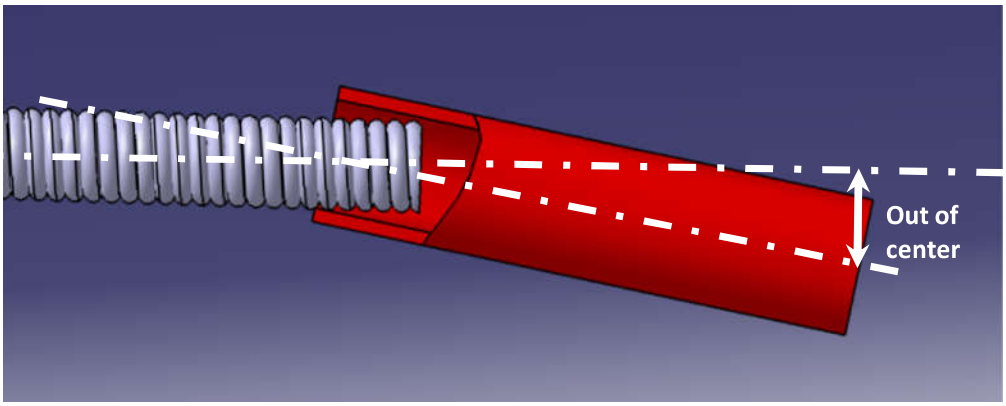

Figure 29: Exaggeration of a possible situation in which cap and TC are not parallel.

3.2.2 Soldering

Gluing and soldering are similar to some extent due to the need for a highly experienced technician and poor repeatability of the process. The latter is mainly due to the difficulty of designing a fixture to keep the cap and torque coil in the exact same place each time since the fixture will be smeared into the solder or glue. This is a problem, especially in sub-millimeter dimensions. Also, due to a small gap between TC and cap, there is a need for keeping some solder or glue on the TC near the joint to ensure secure attachment and strength of the joint (Figure 30-A).

Figure 30: A) Residual solder on the TC, B) oxide formation during soldering on TC and C) flux in solder paste and disappearance of a large portion of paste after heating up.

Thus, the rigid tip of the probe is not always equal to the length of the cap. Depending on the chosen method for cap-TC attachment, it can be more than that (gluing and soldering, Figure 30-A) or equal to it (electroplating and press fitting processes).

The strength of the connection is an encouraging point in choosing this process; however, the main phenomenon that cause problem during the soldering process is unwettability of the stainless steel torque coil, which makes the process a hard choice for TC/Cap connection. During the common soldering process, impurities and oxides form on the TC that makes wettability even

worse (Figure 30-B). Using special fluxes and coating the TC (we made a solder bath for this purpose [24]) can improve wettability, but the process still will be uncontrollable from a symmetry and probe tip length point of view. Solder paste was a potential solution for this problem due to the possibility of applying solder paste in room temperature and controlling the dimensions. However, a big portion of solder pastes are flux (Figure 30-C) and other materials that disappear when the paste is heated up, and the remaining solder in the gap between TC and cap is too small to make a strong connection.

3.2.3 Electrochemical processes

The TC is cut to the required length for each probe and the end is always jagged and not cut fine in case of a mechanical cut (current method). Due to small tolerances (currently 0.04mm between cap and TC) this will cause trouble during the assembling of the TC and the cap. Also, if the chosen tolerances are loose enough to compensate for this defect, it will further affect the symmetry of the probe.

Advanced machining techniques, such as electrochemical machining (ECM) and electro-discharge machining (EDM), are promising processes when there is a need for fine features. However, these are not cheap processes to choose and are not accessible in the lab. Thus, electrochemical etching was considered and applied on the TC end after mechanical cutting. This process can be performed on a batch of TCs and it takes less than 7 minutes which is reasonably fast (Figure 31).

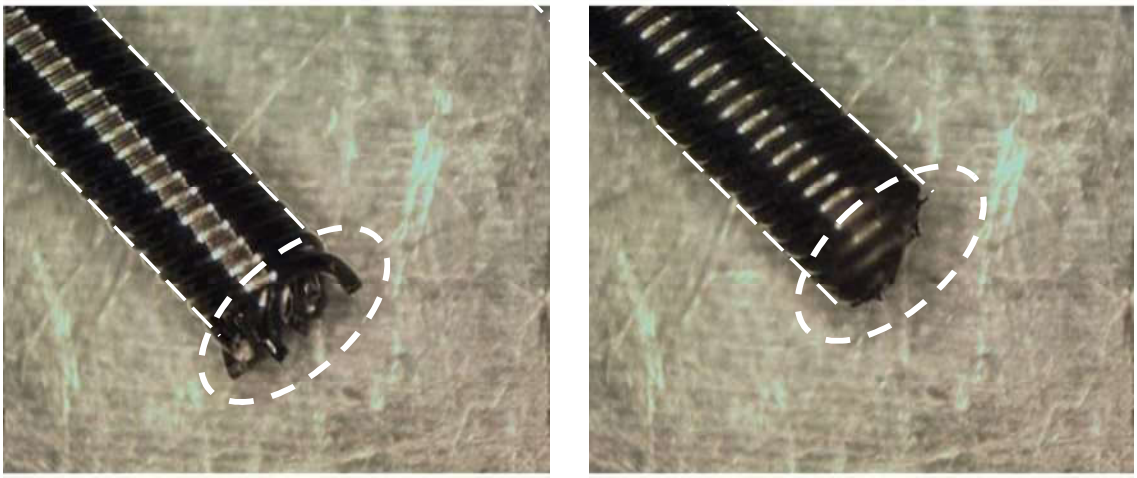

Figure 31: TC A) before and B) after electrochemical etching.

The importance of the electroplating process is due to the controllability of the thickness of joint due to the slow rate of this process. Another advantage of this method is scalability. In case of insulating the sections that are not required to be coated, a batch of probes can be electroplated at the same time, unlike the other three methods that have a one by one approach. The electroplated probe is shown in Figure 32-A.

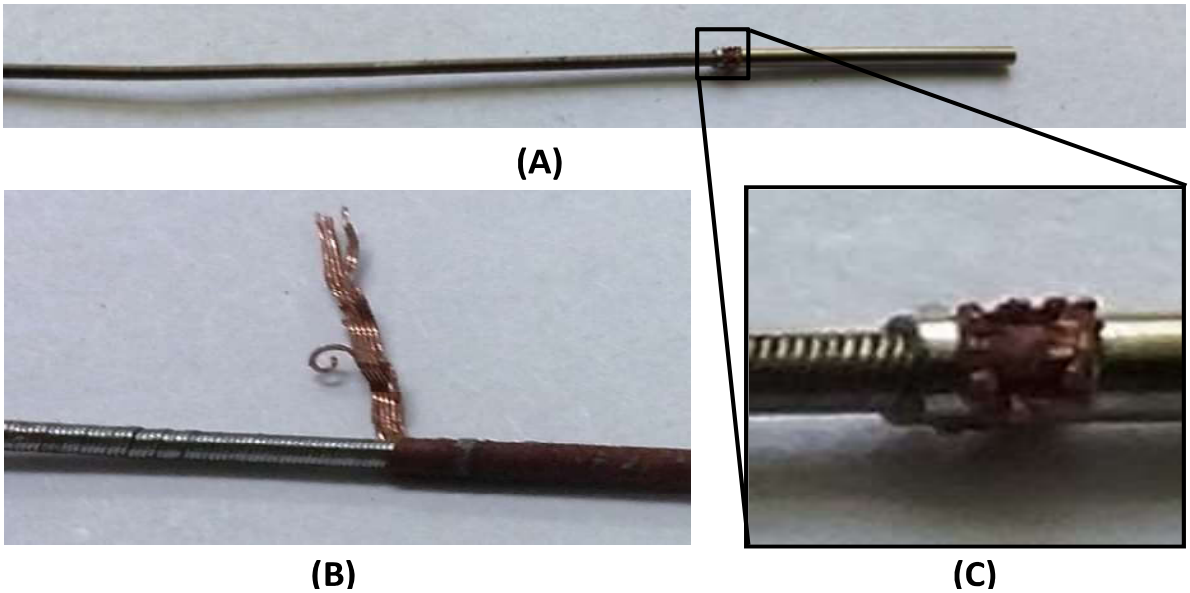

Figure 32: A) Copper electroplated probe, B) demonstration of the ductility of the coated copper and C) clustering of ions on the edges of the cap window.

The coating can be ductile (Figure 32-B); however, the strength of joint is not sufficient for the current application in both nickel and copper plating methods. Also, protecting regions that are not subjected to electroplating and controlling TC and cap interconnection is a difficult task. Ion accumulation on the edges of the window on the cap makes clusters of copper and nickel particles that reduce circumferential uniformity of the joint (Figure 32-C). Although the latter drawback can be less severe in case of reducing the reaction speed, it still remains. These drawbacks resulted in moving on and developing another method for the TC-cap attachment.

3.2.4 Mechanical press fitting

The importance of the press fitting process is that it is the least environmentally hazardous in comparison with soldering, gluing and electroplating. Also, unlike the other three processes, there will be no gap between TC and cap and thus it will not affect the axial symmetry of the probe. Furthermore, the process is pretty fast (typically 40 seconds) and it does not need to be performed under a microscope or by a skilled technician due to a pre-defined setup and designed fixture. And finally, the strength of the joint is high enough for the current application.

The press fitting method is similar to the known crimping process in that it pushes the cap wall towards its center, and by pressing the cap around the TC, it establishes a mechanical frictional contact between the cap and TC. However, unlike a crimping process in which the circumferential uniformity of joint is not of high importance, in the current method an extreme deal of efforts are concentrated on the symmetry and uniformity of the joint for which “press + fitting” can be a more descriptive name. In what follows, the design concepts and designed features are first described. Then results of the simulations are elaborated on and finally the manufactured probes and their important features are described.

3.2.4.1 Design concepts:

In the adjustable six-jaw (ASJ) configuration (Figure 33-A), six moving jaws do the action of pressing and due to the radial movement, this configuration can be flexible in the face of cap diameter changes or small die wear while dimensions of the forming die in fixed two jaw (FTJ) configuration are fixed and do not have this capability. Also, manufacturing of the jaws in the ASJ needs traditional machining processes which makes it less expensive in comparison with FTJ which needs advanced machining such as wire electrical discharge machining. These parameters go hand in hand with the effect of friction in FTJ that causes non-uniformity in circular direction (further discussed in "Simulations" section) and are the main reason for considering ASJ as a promising method and considering it as the focus of experiments.

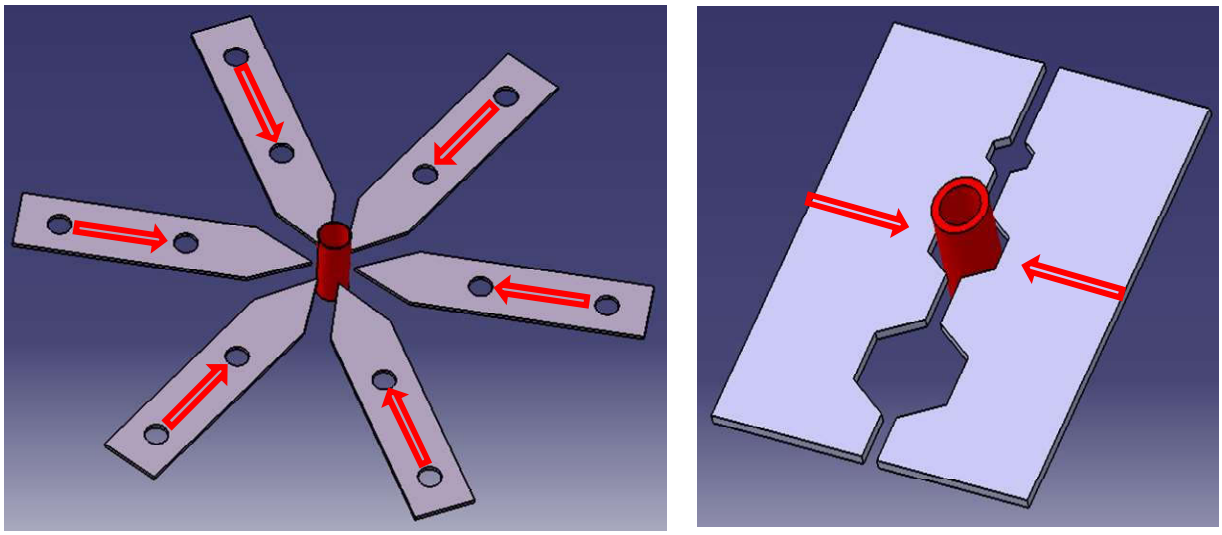

(A) (B)

Figure 33: Two different methods: A) fixed two-jaw and B) adjustable six-jaw forming that are considered and investigated in simulations.

The designed equipment for the ASJ configuration is illustrated in Figure 34. The uniform radial movement of jaws is assured by mounting them on a self-centering lathe chuck (1). 1095 steel sheets of 1mm thickness (2) were machined to a sharp 55 degree arrow shape and the tips are

grinded further to remove the sharpness of the tip and flattened to the designed dimensions. Two Allen screws keep each blade tight on the chuck jaw (3) and the handle (7) is then used to provide the force for pressing the cap

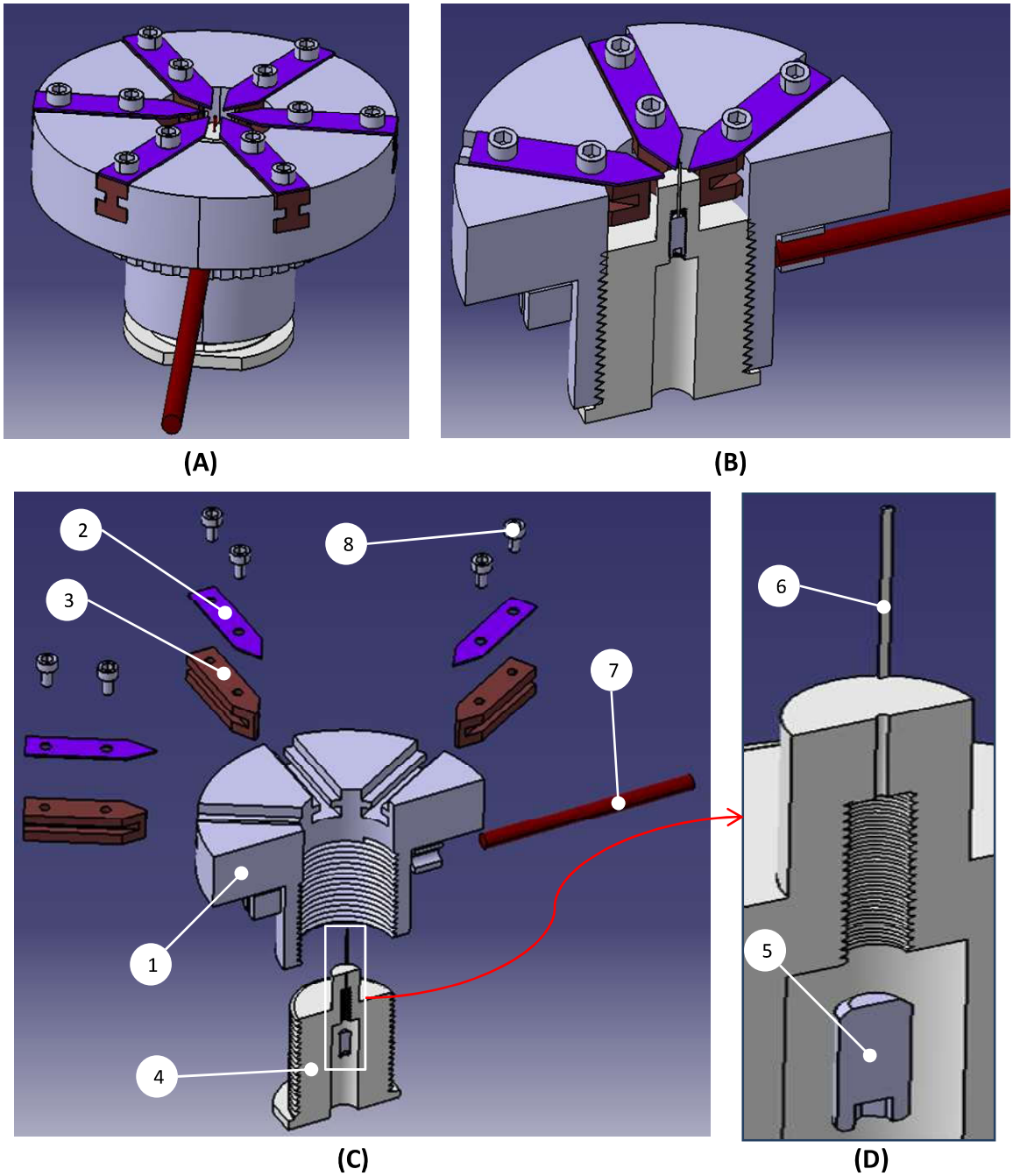

Figure 34: A) Designed equipment, B) cross-section view, C) exploded view of cross-section showing 1) main body (lath chuck), 2) forming 1095 steel blades, 3) mounting jaws, 4) joint position control part, 5) socket head screw controlling cap-TC interconnection, 6) small pin for keeping cap in position, 7) handle for applying pressing force and 8) Allen screws for fastening forming blades on jaws.

Two important features of the design are the joint height and joint length control elements [(4) and (5) in Figure 34-C, respectively]. Through the screw movement mechanism, part (4) defines the position of the pressing on the cap and gives the ability to use it for different probe sizes with different heights. It is demonstrated in Figure 35.

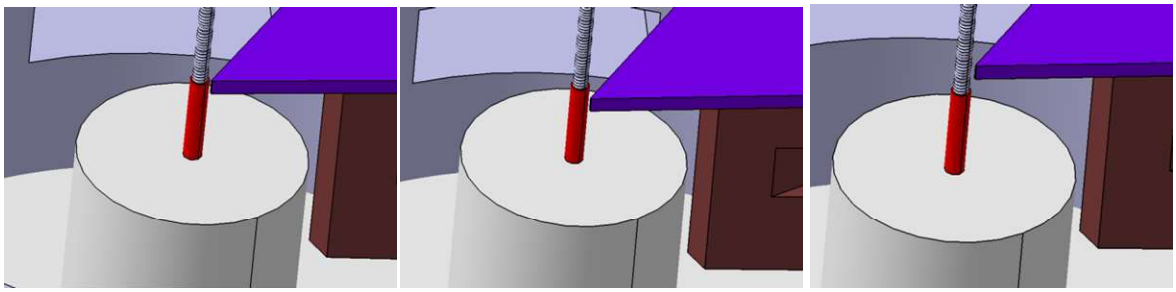

Figure 35: Controlling the position of pressing.

The length of the joint is another important parameter that defines the strength of contact interface on frictional forces. This length is controlled by the socket head screw (5). By turning this screw, the vertical position of the pin (6) is defined that further acts as a stop pin in front of moving the TC into the cap. This pin also keeps the cap and TC in the fixture and, therefore, there is no need to keep the TC or cap in place during the pressing process which makes the process simple and easy to do. Three different positions of the pin that results in three different TC-cap interconnection lengths are shown in Figure 36.

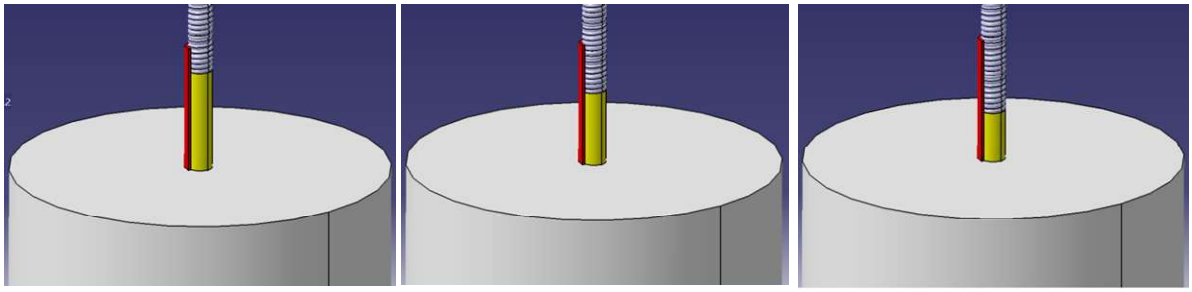

Figure 36: Cap-TC interconnection control.

3.2.4.2 Simulations

The two different configurations (ASJ and FTJ) were simulated. Results were in good agreement with the experiments as are illustrated in the following graphs. In order to double check the validity of the simulations, it is good practice to compare the kinetic and internal energy changes during the process. The kinetic energy being small in comparison with the internal energy (e.g., 7%) is an indication of small analytical error in simulations. These graphs are shown in Figure 37 for both ASJ and FTJ configurations. The kinetic energy is very small in comparison with the internal energy in both cases which is an indication of less error in calculations.

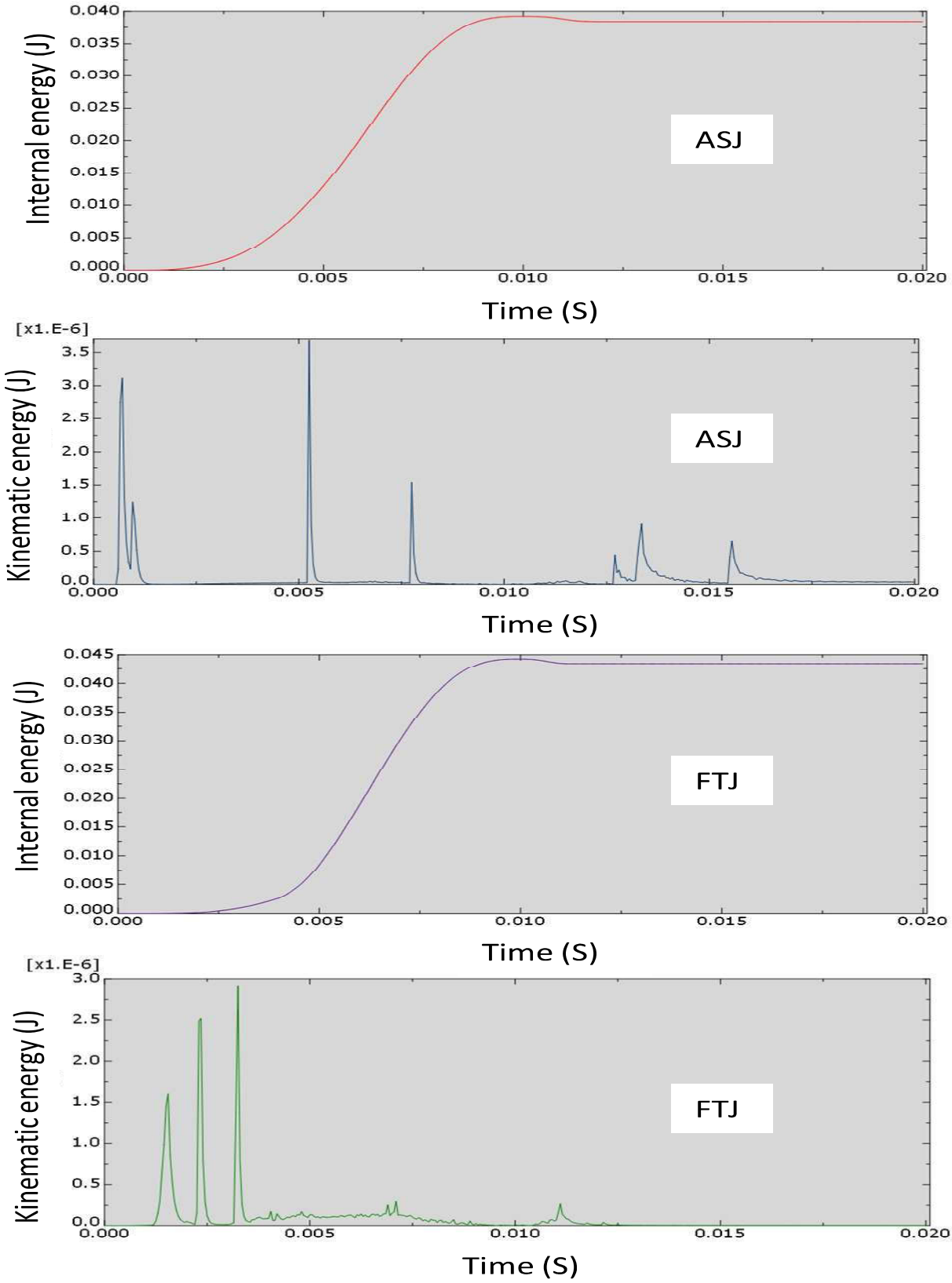

Figure 37: Kinematic and internal energies for both ASJ and FTJ configurations.

An important factor that differentiates between ASJ and FTJ is the effect of frictional forces on the specimen. As is demonstrated in Figure 38, the friction on FTJ is pushing the material towards the edges. This results in wrinkling of the material on the cross-section where two pairs of die are touching each other in FTJ (Figures 38-A&B). It will result in non-uniformity in the radial direction. On the other hand, frictional forces on jaws in the ASJ configuration are symmetric and it results in a uniform circumferential shape (Figure 38-C).

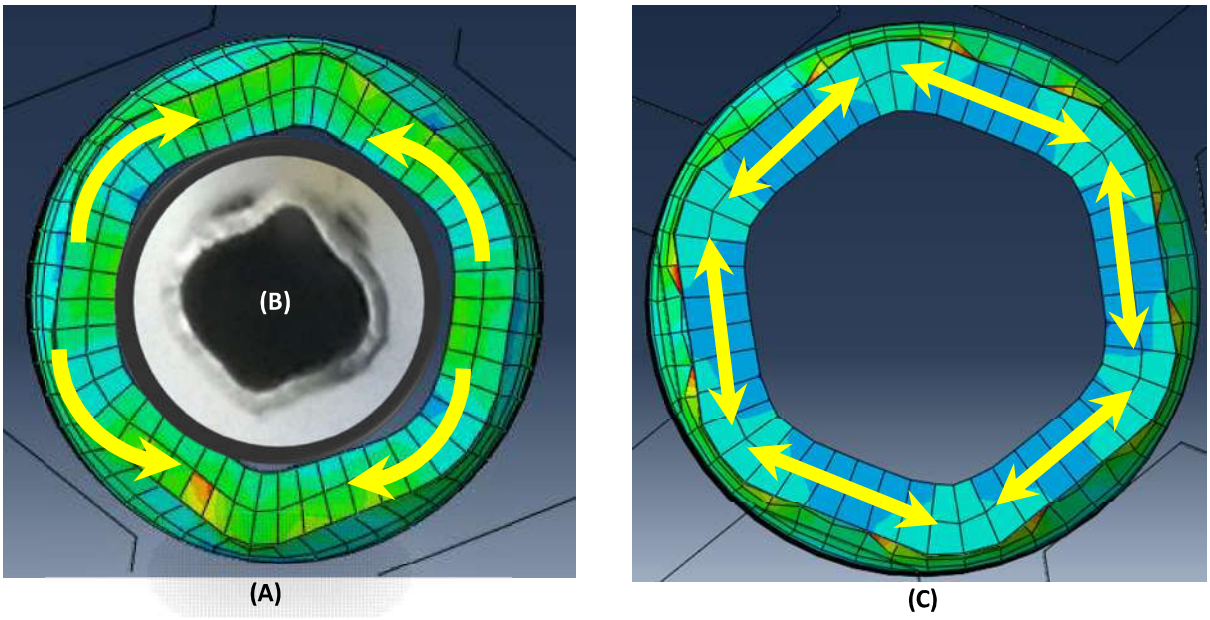

Figure 38: Friction acting on tooling in FTJ (A) and ASJ (C). The actual work piece deformation in FTJ is shown in part (B).

The maximum stress in the FTJ is about 70 MPa (8%) more than the ASJ method. This difference results in a more plastic (permanent) deformation on certain portions. Considering the small thickness of the cap and non-uniform distribution of stresses, this approach will be more prone to wrinkling of the cap. Forming processes in the press fitting methods and typical stress distribution are shown in Figure 39.

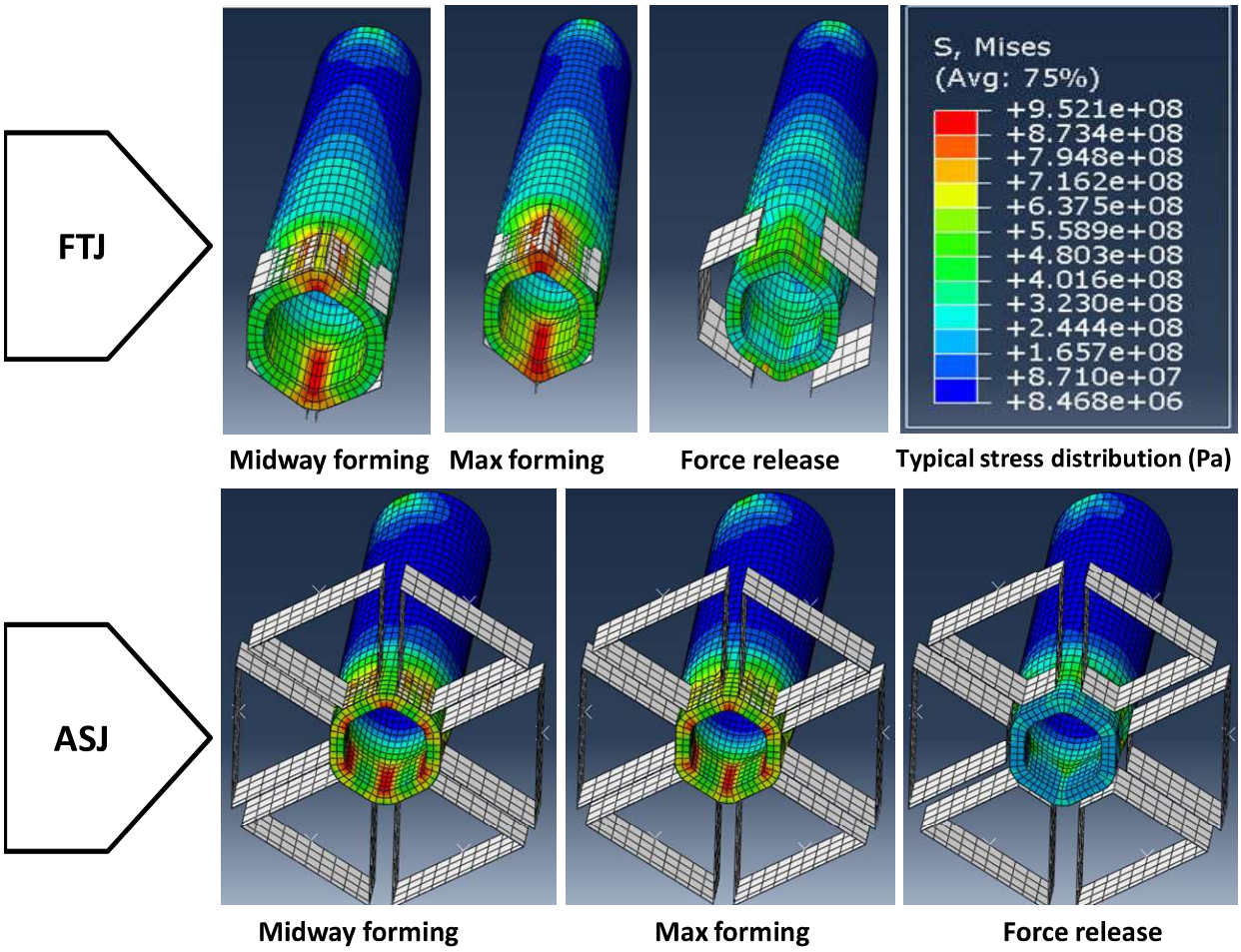

Figure 39: Finite element simulation of FTJ and ASJ configurations.

Affected length and maximum radial distance of the joint portion of the cap are two other important aspects. The affected axial length of the cap is roughly about 10 % of the joint length in the press fitting process while it can be about 100% or more in the gluing and soldering processes. Also, the maximum distance of the joint portion from the center of the TC can be more than the radius of the cap in soldering, gluing and electroplating methods. This amount is less than the cap radius in both FTJ and ASJ configurations in the press fitting method as is shown in Figure 38. Affected length and maximum radial distance of the joint portion are not repeatable and not well controlled for the soldering and gluing approaches which make them less reliable. They are both predictable and repeatable for the press fitting method (Figure 40).

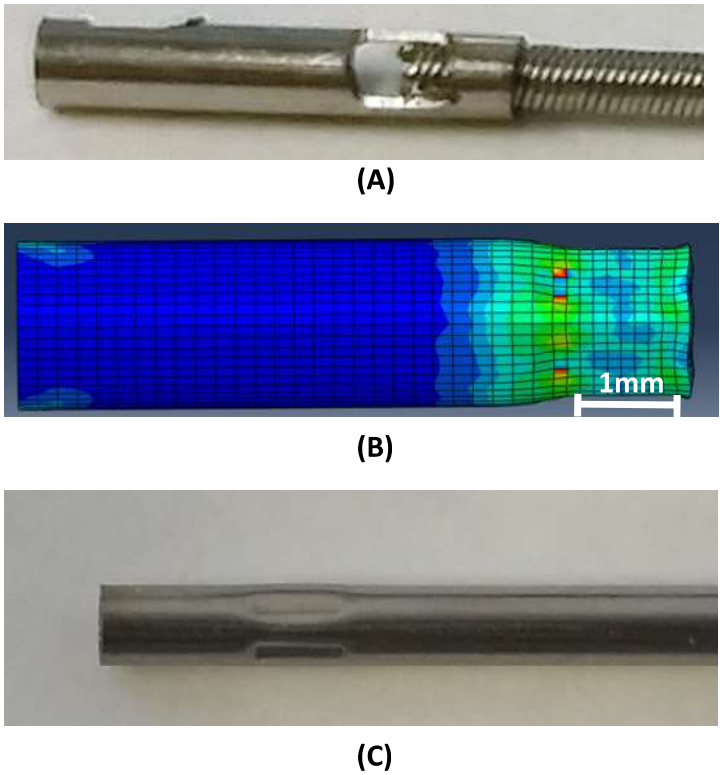

Figure 40: A) Manufactured probe, B) illustration of joint length and affected portion of the cap and C) the severe deformation of cap for exaggerating the joint length and affected area.

3.2.4.3 Experiments

An interesting phenomenon that happens during the press fitting is the spring back of the cap. This is a well known process in metal forming, especially the forming of sheet metals [25]. This assists in leaving enough space for the optical fiber to move freely in the probe tip.

The amount of force applied to detach the TC from the cap is an extremely important factor in the manufacturing of probes. The press fitting method has already shown enough proof for considering it as a necessary process in the manufacturing of probes with a cap-TC configuration, even if a further soldering or gluing is important. It is due to the important role of the press fitting in keeping the cap and TC parallel and concentric. However, for the current probes (1.27 mm cap and 0.94mm TC), a one pound resistance was reached for five consecutive

samples. This clearly shows the efficiency of press fitting process by itself as an attachment method without need for further processing.

Non-uniformity in circumference is a problem which is currently observed in some samples. This is mainly due to uncontrolled radial force that can cause wrinkling in case of excessive force. This problem is easily controllable using a torque meter or a physical stop to prevent the handle [(7) in Figure 34-C] from excessive rotation.

4 CONCLUSION AND FUTURE WORK

A series of analytical and experimental investigations were conducted in the current study to improve the quality of images distorted due to NURD and also to improve the quality of the probes and thus eliminate the occurrence of NURD in the first place.

The theoretical work included two main sections. The first part was focused on providing the MATLAB code for reconstructing the results of paper which contained a developed dynamic programming method for post-processing the data with respect to the NURD correction. The MATLAB coding had two figurative and quantitative outputs which could well correct the distortion of images. The quantitative method based on standard deviation of pixels intensity from the mean value was a method of validation of applied corrections. The light load of the code and fast analytic time were among the important features of this code.

The second part of the theoretical work was focused on finite element simulation of the press fitting process to investigate the effect of two tooling configurations on the circumferential uniformity of the probe. Considering a hexagonal cross-section for the joint, simulation of adjustable six-jaw (ASJ) and fixed two-jaw (FTJ) configurations revealed the important effect of friction on the uniformity of the joint and showed the superiority of ASJ method.

Experimental efforts were mainly focused on developing a method for attaching the Torque Coil (TC) to the cap which can secure three important features of axial symmetry, short rigid length of the probe tip and the mechanical strength. Four different methods, namely gluing, soldering, electroplating and mechanical press fitting, were considered and their pros and cons were described.

In the soldering and gluing processes, the rigid length of the probe tip is not easy to control due to unavoidable residual solder or glue on the TC. The axial symmetry of the probe is another important parameter that currently is not fully controllable in these two methods. These two drawbacks can introduce errors and make the manufacturing process not repeatable and therefore not reliable. In the electroplating method, due to the slow speed of the plating process, the thickness of coating is controllable, and it can be circumferentially uniform. Also, a batch of probes can be processed at the same time which can save time and money for the manufacturer. However, protecting areas other than the joint area, providing the fixture for controlling the TC-cap joint length, and the strength of the joint were three main difficulties that hindered application of this method for the current probes. In all methods mentioned above, concentricity of TC and cap are not controllable which can cause them to be out of center and/or non-parallel.

The press fitting method is a promising process in that it is clean, fast, repeatable and strong. In this method, no chemicals or environmentally hazardous material is used. Also, the whole process takes place in less than one minute, and there is no need to use a microscope and skilled personnel which reduces the cost of probe making. Due to using a fixture that controls the joint length (1.5mm) and its location, the method is repeatable and thus reliable. Also, the length of affected area is insignificant (0.1 - 0.2 mm) and together with the short joint length helps reduce the rigid length of the probe tip. Since during the press fitting the gap between TC and cap no longer exists, TC and cap will be parallel and concentric.

Future work will be focused on considering additional features in the press fitting equipment design for applying controlled loads and calibrating the equipment. Also, the developed code for the NURD correction will be tested on more sets of data and additional features will be considered for improving the functionality of the algorithm.

References

1. Roleder, T., et al., *The basics of intravascular optical coherence tomography.* Postępy w Kardiologii Interwencyjnej = Advances in Interventional Cardiology, 2015. **11**(2): p. 74-83.
2. Elbau, P., L. Mindrinos, and O. Scherzer, *Mathematical Methods of Optical Coherence Tomography*, in *Handbook of Mathematical Methods in Imaging*, O. Scherzer, Editor. 2015, Springer New York: New York, NY. p. 1169-1204.
3. Bezerra, H.G., et al., *Intracoronary Optical Coherence Tomography: A Comprehensive Review.* Clinical and Research Applications, 2009. **2**(11): p. 1035-1046.
4. *Intravascular Imaging: OCT and IVUS.* Interventional Cardiology Clinics, 2015. **4**(3): p. viii.
5. Motreff, P., et al., *High-resolution coronary imaging by optical coherence tomography: Feasibility, pitfalls and artefact analysis.* Archives of Cardiovascular Diseases, 2010. **103**(4): p. 215-226.
6. Soest, G.v., J.G. Bosch, and A.F.W.v.d. Steen, *Azimuthal Registration of Image Sequences Affected by Nonuniform Rotation Distortion.* IEEE Transactions on Information Technology in Biomedicine, 2008. **12**(3): p. 348-355.
7. Uribe-Patarroyo, N. and B.E. Bouma, *Rotational distortion correction in endoscopic optical coherence tomography based on speckle decorrelation.* Optics letters, 2015. **40**(23): p. 5518-5521.
8. Sinclair, H., et al., *OCT for the Identification of Vulnerable Plaque in Acute Coronary Syndrome.* JACC: Cardiovascular Imaging, 2015. **8**(2): p. 198-209.
9. Mancuso, J.J., et al., *Intravascular optical coherence tomography light scattering artifacts: merry-go-rounding, blooming, and ghost struts.* Journal of Biomedical Optics, 2014. **19**(12): p. 126017.
10. Suter, M.J., et al., *Optimizing flushing parameters in intracoronary optical coherence tomography: an in vivo swine study.* The international journal of cardiovascular imaging, 2015. **31**(6): p. 1097-1106.

11. Kawase, Y., et al., *Comparison of nonuniform rotational distortion between mechanical IVUS and OCT using a phantom model.* Ultrasound in Medicine & Biology, 2007. **33**(1): p. 67-73.
12. Ahsen, O.O., et al., *Correction of rotational distortion for catheter-based en face OCT and OCT angiography.* Optics Letters, 2014. **39**(20): p. 5973-5976.
13. Herz, P.R., et al., *Micromotor endoscope catheter for in vivo, ultrahigh-resolution optical coherence tomography.* Optics Letters, 2004. **29**(19): p. 2261-2263.
14. Li, J., et al., *High speed miniature motorized endoscopic probe for optical frequency domain imaging.* Optics Express, 2012. **20**(22): p. 24132-24138.
15. Gatta, C., et al., *Fast Rigid Registration of Vascular Structures in IVUS Sequences.* IEEE Transactions on Information Technology in Biomedicine, 2009. **13**(6): p. 1006-1011.
16. Sathyanarayana, S., *Nonuniform rotational distortion (nurd) reduction*. 2008, Google Patents.
17. Kang, W., et al., *Motion artifacts associated with in vivo endoscopic OCT images of the esophagus.* Optics Express, 2011. **19**(21): p. 20722-20735.
18. Ughi, G.J., et al., *Automatic three-dimensional registration of intravascular optical coherence tomography images.* Journal of Biomedical Optics, 2012. **17**(2): p. 0260051-02600511.
19. Dufour, M.L., et al. *Tools for experimental characterization of the non-uniform rotational distortion in intravascular OCT probes*. 2011.
20. Kleemola, H.J. and M.A. Nieminen, *On the strain-hardening parameters of metals.* Metallurgical Transactions, 1974. **5**(8): p. 1863-1866.
21. R, L.G., *Electroplating pipe joint*. 1956, Google Patents.
22. Mattia, M. and H.D. Van Sciver, *Method of joining dissimilar metals by plating*. 1972, Google Patents.
23. Martín, M.M., *Chapter 2 - Chemical processes*, in *Industrial Chemical Process Analysis and Design*. 2016, Elsevier: Boston. p. 13-60.
24. Puttlitz, K.J. and K.A. Stalter, *Handbook of Lead-Free Solder Technology for Microelectronic Assemblies*. 2004: Taylor & Francis.
25. E, D.-x., et al., *Spring-back deformation in tube bending.* International Journal of Minerals, Metallurgy and Materials, 2009. **16**(2): p. 177-183.